ORIGINAL

D. Brands · D. Balzani · L. Scheunemann · J. Schröder ·
H. Richter · D. Raabe

Computational modeling of dual-phase steels based on representative three-dimensional microstructures obtained from EBSD data

Abstract The microstructure of dual-phase steels consisting of a ferrite matrix with embedded martensite inclusions is the main contributor to the mechanical properties such as high ultimate tensile strength, high work hardening rate, and good ductility. Due to the composite structure and the wide field of applications of this steel type, a wide interest exists in corresponding virtual computational experiments. For a reliable modeling, the microstructure should be included. For that reason, in this paper we follow a computational strategy based on the definition of a representative volume element (RVE). These RVEs will be constructed by a set of tomographic measurements and mechanical tests. In order to arrive at more efficient numerical schemes, we also construct statistically similar RVEs, which are characterized by a lower complexity compared with the real microstructure but which represent the overall material behavior accurately. In addition to the morphology of the microstructure, the austenite–martensite transformation during the steel production has a relevant influence on the mechanical properties and is considered in this contribution. This transformation induces a volume expansion of the martensite phase. A further effect is determined in nanoindentation test, where it turns out that the hardness in the ferrite phase increases exponentially when approaching the martensitic inclusion. To capture these gradient properties in the computational model, the volumetric expansion is applied to the martensite phase, and the arising equivalent plastic strain distribution in the ferrite phase serves as basis for a locally graded modification of the ferritic yield curve. Good accordance of the model considering the gradient yield behavior in the ferrite phase is observed in the numerical simulations with experimental data.

D. Brands (✉) · L. Scheunemann · J. Schröder
Abteilung Bauwissenschaften, Fakultät für Ingenieurwissenschaften, Institut für Mechanik, Universität Duisburg-Essen,
Universitätsstraße 15, 45141 Essen, Germany
E-mail: dominik.brands@uni-due.de

D. Balzani
Fakultät für Bauingenieurwesen, Institut für Mechanik und Flächentragwerke, TU Dresden, Dresden, Germany

H. Richter
ThyssenKrupp Steel Europe AG, Technologie and Innovation, TIS-AT-UT Umformtechnik, Dortmund, Germany

D. Raabe
Department of Microstructure Physics and Alloy Design, Max-Planck-Institut für Eisenforschung, Düsseldorf, Germany

1 Introduction

In many fields of steel applications, e.g., automotive engineering or manufacturing, the optimization of the material properties becomes one of the main challenges. The reduction of weight as well as an increasing stability and crash safety are main driving forces. Consequently, in the last four decades several new steel types have been developed and are represented by the group of advanced high- strength steels (AHSS). One important AHSS is the dual-phase (DP) steel, and other well-known types are transformation induced plasticity, complex phase or martensitic steels. First developments of especially the DP steels showing greater formability than conventional steels go back to the 1970s, see, e.g., [45] and [20]. For the production of DP steels, the hot-rolled steel is processed by a controlled cooling from its high-temperature austenite or austenite–ferrite state. This rapid cooling enforces the transformation from austenite to martensite. In the end, the microstructure consists of a ferritic matrix phase with martensitic inclusions of complex shape. Controlling the transformation is the crucial part of the adjustment of the mechanical properties of the final product. A variety of publications have shown that this behavior mainly depends on microstructure factors such as volume fraction, shape, size, spatial distribution, and the carbon content of the martensite phase, see, e.g., [5,19,20,39,41,42,52,63,90].

For the improvement in the properties of DP steels the microstructural composition as mentioned above plays an essential part. A technique to measure polycrystalline microstructures is electron backscatter diffraction (EBSD). Thereby, an electron beam is focused on the examination sample and the diffracted electrons form a two-dimensional pattern on a fluorescent screen. From this pattern the crystal structure and orientation can be characterized. One application of EBSD is the determination of recrystallization states and their influence on the mechanical properties of DP steels, cf. [12,15,18,29,65,70,86]. An extension of the EBSD technique to obtain three-dimensional information is done by a combination of the EBSD with a serial sectioning by a focused ion beam (FIB) system and results in a set of cross-sectional information, see [44,102]. In case of DP steels the different phases cannot be distinguished by the crystallographic pattern produced by the EBSD. Thus, a further measure captured in the EBSD analysis, the image quality also referred to as diffraction pattern quality, describes the quality of the resulting EBSD pattern. Based there on [96] show the correlation of low image-quality values to the occurrence of martensite, see also [99]. This is used by several contributions to analyze volume fraction, morphology, and distribution of the martensitic inclusion phase of DP steels, see, e.g., [35,36,97,98,100]. For the improvement in the representativity of the EBSD measurement especially the phase fraction determination [21] propose a new EBSD scanning scheme with a two-step size movement of the electron beam. Its improvements toward the EBSD-based texture analysis was shown in [22].

The increase in computational performance has enabled the analysis and modeling of the mechanical properties as well as the simulation of DP steel applications, see, e.g., [87,88]. Due to the importance of the microstructural assembly of the martensite in the ferrite phase, most publications on the analysis of the DP steel behavior base on micromechanical models. The analysis of the mechanical properties considering different physical aspects of the individual phases, i.e., ferrite and martensite, are reported in, e.g. [37,40,50,62,85].

One physical aspect, which will be also considered in the following, is the volume expansion of the inclusion phase during the production process due to transformation of austenite to martensite. This effect is also considered in the contributions by, e.g., [38,64,77,93].

For the simulation of real microstructures, as also done in the references given above, suitable techniques for the reconstruction of the microstructure morphology and its transformation into computationally useable models, e.g., in the context of finite element discretizations, are necessary. Most available methods base on the acquisition of information about the microstructural composition by, e.g., EBSD or scanning electron microscopy (SEM) and obtain reconstructions by image processing tools, cf. [11,14,30,31,92]. Furthermore in most of the micromechanical analysis, the macroscopic response of the DP steel is also of interest. In general, this macroscopic behavior is computed by suitable volume averages over the considered microstructure, which is often only a small sample of the full material. In order to obtain a representative result with respect to the overall material behavior, the considered sample must be a representative volume element (RVE). The RVE is considered to be a partial volume of the material, which is statistically homogeneous from the macroscopic point of view, cf., e.g., [25,32,34,60,84] and for a summary [103], where definitions for RVEs are discussed.

The use of parts of a real microstructure as RVE often results in numerical drawbacks due to their geometrical complexity and the resulting large number of degrees of freedom in the computational model. In reference to the applied numerical methods, the efficiency for the prediction of the macroscopically mechanical response can be increased by using more efficient computational methods. For example [49] and [26] use the Fast Fourier transform method and the spectral method, respectively, to compute the average mechanical response of microheterogeneous materials. Contrarily, the construction of simplified geometrical models is the aim

of, e.g., [1–3], where an axisymmetric RVE cell is constructed based on morphological properties. Further methods for the construction of RVEs based on three-dimensional Voronoi tessellation, e.g., [24], and on the application of the Monte Carlo technique, e.g., [17]. Further techniques have been suggested in order to reproduce the statistical distribution of grain size and shape obtained from experimental observations of two-dimensional orthogonal sections, cf., e.g., [13] and [83]. In [68,69,72] the three-dimensional characterization of DP steels result in statistically representative three-dimensional microstructures. An alternative approach is the construction of statistically similar RVEs (SSRVEs), cf. [6]. These SSRVEs are characterized by a lower complexity compared to the real microstructure, but they represent the overall material behavior accurately enough. The reliability of this method especially for DP steel microstructures was shown in, e.g., [4,7,8,78]. For an extension of this method to 3D see [9] and for the construction using Minkowski Functionals as statistical descriptors we refer to [73].

In this paper the computational modeling of DP steels based on representative three-dimensional microstructures is presented, which should be representative in the sense of reproducing the mechanical response of real experiments. In detail the paper is organized as follows: Sect. 2 gives an overview of the techniques used for the metallographic characterization of the considered DP steel. The processing of the metallographic data to reconstructions of the microstructure is given in Sect. 3. In Sect. 4, the three-dimensional reconstructions are statistically and mechanically analyzed with respect to reference data. The construction and enhancement of statistically similar volume elements for DP steel simulation are described in Sect. 5, and the paper is concluded in Sect. 6.

2 Measurements of microstructure based on EBSD

For the metallographic characterization, we use data resulting from the 3D electron backscatter diffraction (3D EBSD) method. Thereby a joint high-resolution field emission SEM/EBSD setup is coupled with a focused ion beam system (FIB). It provides a set of cross-sectional planes obtained via sequential serial sectioning and joint EBSD phase and texture mapping. The dual-beam setup (SEM,FIB) is shown in Fig. 1a, b.

The sample of the material, which should be treated, is mounted on a tiltable holder inside the microscope, cf. Fig. 1b. During the investigation, the sample is tilted between two positions, i.e., the FIB-cutting and the EBSD positions. In the cutting position, the FIB system mills thin layers (10 nm - 1 µm thick) from the investigated surface of the sample. The other position is used for the EBSD analysis, where an electron beam is focused on the milled surface and the back scatter diffraction patterns are monitored by the EBSD camera. In order to reduce lattice damage that can be created by the ion milling procedure during the sequential cutting operations, we used comparably low cutting rates, i.e., sufficiently small beam current values. Due to different diffraction patterns several properties of the sample can be analyzed for each point, e.g., crystal orientation, phase, and internal lattice distortion. The typical EBSD dataset covers, e.g., the specific in-plane coordinates for measured points in the cross-section, where the Euler angles characterize the crystallographic orientation, and the image quality indicates the defect-density-dependent quality of the diffraction pattern. Concerning the

(a)   **(b)**
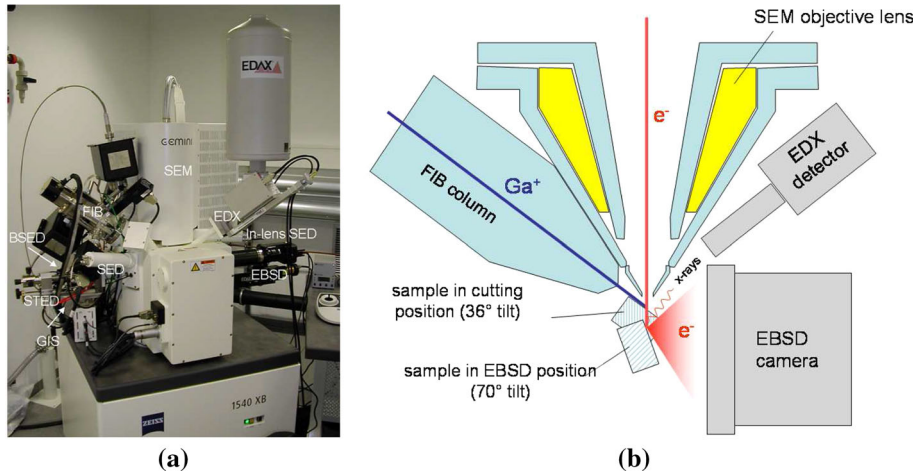
Fig. 1 EBSD–FIB: **a** equipment, **b** technical setup, cf. [44]
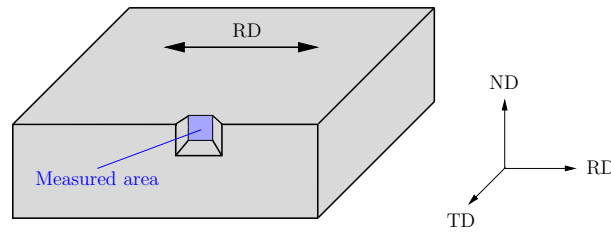
Fig. 2 Measured area in sheet metal with rolling direction (*RD*), transverse direction (*TD*) and normal direction (*ND*)

**Table 1** Physical size and in-plane step size of 3D EBSD data sets

	In-plane step size (μm)	# of slices (μm)	Distance slice-to-slice (μm)	Size of data set in		
				RD(μm)	ND(μm)	TD(μm)
Slicescan 1	0.1	50	0.1	15.9	16.45	5
Slicescan 2	0.1	97	0.1	21.6	20.78	9.7

3D EBSD method we refer to [23,44,101,102]. Since here we make use of the image-quality values to identify and digitalize the different DP steel phases, we also refer to [16,99] regarding the mapping of this quantity. Irrespective of minor beam damage, however, the use of the image quality to differentiate between the ferrite and the martensite phases is a sufficiently clear parameter: The intrinsic distortion of the martensite obtained from the preceding quenching process is so profoundly larger than that of the ferrite, even when being exposed to a certain degree of ion beam damage, that the two phases can be very well differentiated from each other.

Here, we focus on the analysis of microstructures of DP steel sheets. On that account in Fig. 2 the area measured by EBSD and its orientation with respect to the sheet metal directions are shown. The rolling direction (RD) is equal to the longitudinal one, the transverse direction (TD) is in line with the width of the sheet, and the thickness direction equals the normal direction (ND). The milling using the FIB results in cutting planes parallel to the RD–ND plane, while the electron beam of the EBSD works within these planes at a certain step size for its in-plane movement. Consequently, the resulting datasets of the EBSD measurement are associated with planes arranged along the TD axis. In this paper, we analyze two 3D EBSD datasets, which are in the following referred to as *Slicescan 1* and *Slicescan 2* with the physical information given in Table 1.

In the following we investigate the representativity of reconstructions of the microstructures. For this purpose we make use of a special technique for EBSD measurements to obtain a large area scan. This technique was originally proposed by [21] for the determination of phase fraction in multiphase materials. Its improvements toward the EBSD-based texture analysis was shown in [22].

This technique is based on a new EBSD scanning scheme, which in contrast to the 3D EBSD method performs a measurement only in one plane. It is mainly characterized by the stepping of the in-plane movement of the electron beam. The beam is moved in a two-step size mode: the large step size (here 500 μm) indicates a coarse grid, at which the beam probes areas with a small step size (here 0.1 μm). In our case a coarse grid of 32×4 points in the RD-ND-plane is considered, where at each point the probed (small) area is 15 μm $\times$ 15 μm in size, cf. Fig. 3. Thus, a sufficiently large area (16 mm $\times$ 2 mm) of the considered DP steel is covered to estimate representative statistical properties, e.g., phase fraction. Hereafter, this dataset is referred to as *Largescan*.
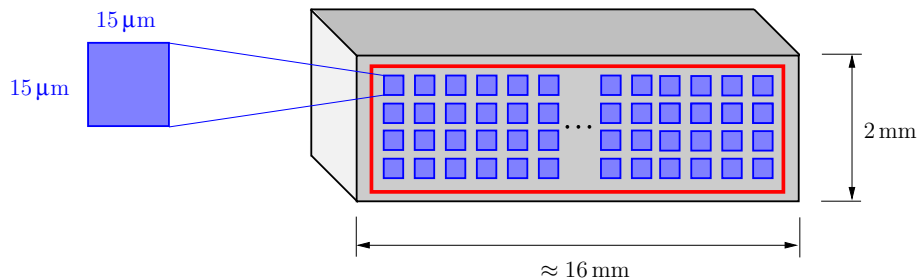
Fig. 3 Illustration of the measurement approach used for the *Largescan* data. Here we consider a coarse grid of 32×4 pattern

3 Processing of EBSD data for phase reconstructions

For the computational modeling of DP steels including microstructural information, a reconstruction of the microstructure is needed. Here, a reconstruction with respect to the different phases, which are mainly a ferrite matrix with embedded martensite inclusions, is considered. In this section, first the method used for the 2D reconstruction of a microstructure based on an EBSD dataset is presented. Subsequently, the results obtained by applying this reconstruction method to the measurements described in Sect. 2 are shown. Consequently, from the *Largescan* a set of 2D phase reconstructions is achieved and the *Slicescan 1* and *Slicescan 2* result in three-dimensional phase reconstructions serving as basis for the finite element computations in this paper.

3.1 Reconstruction method

The basis for the microstructure reconstruction is the image-quality factor $Q(x, y)$ obtained at each measurement point of a two-dimensional EBSD map. Wilkinson and Dingly [96] show, that the image-quality factor can be related to the intensity of the stored defect density obtained from plastic deformation and stress. For example, [98] and [100] have exploited this fact for the phase identification in DP steels and found that high image-quality factors correlate with ferrite and low factors correlate with martensite.

Wu et al. [100] also suggest to normalize the image-quality values, because they are sensitive to the EBSD processing parameters. Accordingly, we compute the normalized image quality values for each 2D EBSD measurement by

$$Q_{\text{normal}}(x, y) = \frac{Q(x, y) - \min_{x,y}(Q)}{\max_{x,y}(Q) - \min_{x,y}(Q)} \cdot 100 , \tag{1}$$

The resulting values are in the range [0, 100]. Figure 4a shows an example, where the grayscale map of the normalized image-quality values Q_{normal} is shown for one 2D EBSD dataset of the *Largescan* measurement. Therein the higher image-quality values (brighter regions) and the lower ones (darker regions) are associated with ferrite and martensite, respectively.

The next step is the definition of a suitable threshold value of the normalized image quality to distinguish between the ferrite and martensite phase. Note, that the value of the threshold is correlated with the resulting phase fractions in the reconstructions, cf. [98]. Thus, the mechanical response obtained by using the reconstructions in numerical computations will be also influenced by the choice of the threshold. Motivated by [98], we compute the histogram of the image quality values, where we divide the full range into 50 categories with the category length $\Delta l = 2$. By counting all image quality values Q_{normal} within category i, we obtain the frequency distribution $h(i)$. From these values we compute the probability density function (PDF)

$$f(i) = h(i) \Big/ \left[\sum_{j=1}^{50} h(j) \, \Delta l \right] \quad \text{for} \quad i = 1, \dots 50 , \tag{2}$$

where $f(i) \cdot \Delta l$ denotes the probability of Q_{normal} to be in the category i. For the grayscale map in Fig. 4a, the PDF is plotted in Fig. 4c. The graph shows a bimodal distribution of Q_{normal}, i.e., the histogram shows two maxima at category 30 and 84 with a minimum in between, which is comparable with the results obtained by [98]. They can be described by the superposition of two standard normal distributions also known as Gaussian function, cf. [100] and [18]. Each function of these distributions is obtained by an iterative least-squares fit using the MATLAB peakfit function by [58]. On that account we divide the whole PDF in two data segments at the position of the minimum between both peaks, i.e., lowest value between the maxima. Then the standard normal distributions are fitted separately to each of these PDF data segments. The resulting functions are also plotted in the graph shown in Fig. 4c, where the green and red lines indicate the standard distribution functions for the martensite (left) and the ferrite (right) peak, respectively. Then the final threshold $Z_{Q_{\text{normal}}}$ is estimated at the intersection point of both the peak functions, which is indicated by a 'o' at the category axis in Fig. 4c. With this threshold, we are able to reconstruct the binary representation of the microstructure by assigning a measured point with $Q_{\text{normal}} \leq Z_{Q_{\text{normal}}}$ to the martensite phase and a point with $Q_{\text{normal}} > Z_{Q_{\text{normal}}}$ to the ferrite phase. The resulting binary phase reconstruction for the considered microstructure (Fig. 4a) is shown in Fig. 4b.

From the comparison of the grayscale image-quality map in Fig. 4a and the corresponding phase reconstruction one can directly observe two problems associated with the identification of the phases, which are also mentioned by [18]:
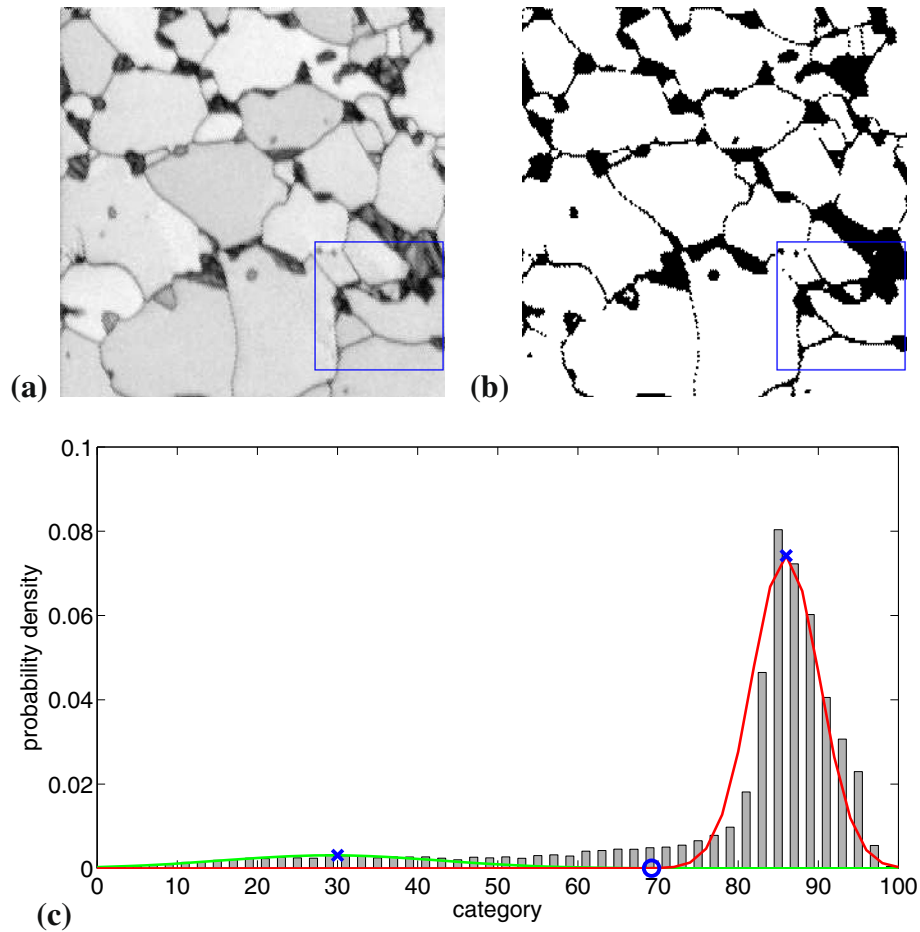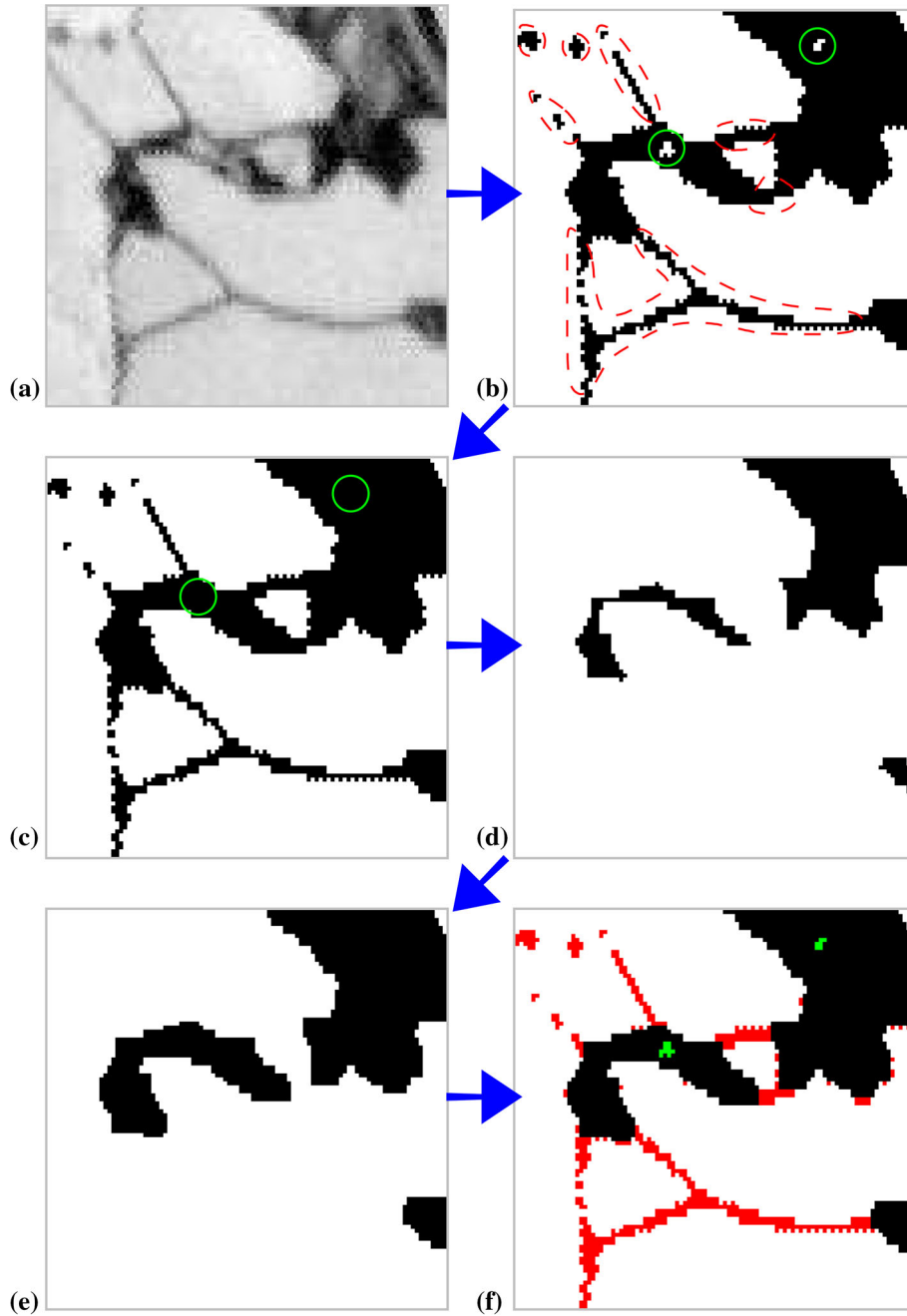
Fig. 4 a The *grayscale* image-quality map of a DP steel microstructure and **b** the corresponding binary image of the phase reconstruction (*black* = martensite, *white* = ferrite) using the threshold, which is determined from **c** the probability density function of the normalized image-quality factor $\mathcal{Q}_{normal}$ (*green line/red line* fitted standard normal distribution, *open circle* intersection point, *times symbol* peaks if standard normal distribution). The *blue frame* in **a** and **b** represents the region, which serves as example for the description of the reconstruction method. The underlying microstructure in **a** and **b** is 15 μm × 15 μm in size and the *blue frame* covers a region of 5 μm × 5 μm. (Colour figure online)

- Very small and possibly unrealistic islands identified as ferrite phase appear inside martensite inclusions which lead to unnecessarily fine discretizations when constructing a finite element mesh for the microstructure. The much stiffer mechanical behavior of martensite at stress levels typically occurring in sheet metal forming would, however, essentially prevent any plastic deformation in these ferrite regions.
- Several thin structures appear in the reconstruction, cf. Fig. 4a, which can be identified as ferrite-to-ferrite grain boundaries comparing the grayscale image-quality map with the phase reconstruction. Due to the different crystal orientations in neighboring grains and the higher defect density at the grain boundaries, the image-quality factor is also lower compared to regions inside the grains. Consequently, the grain boundaries might be identified as martensite phase. Since we are interested in a two-phase reconstruction of the microstructure the grain boundaries between two ferrite grains should also be assigned to the ferrite phase.

For a better understanding of the aforementioned aspects, we select a smaller region of the considered microstructure. This region is indicated by a blue frame in Fig. 4a, b and is shown in Fig. 5a. In Fig. 5b the binary image of the phase reconstruction is shown, which is obtained from applying the image-quality threshold value and which is identical to the blue frame in Fig. 4b. In addition, we mark the regions associated with ferrite islands by green circles. For the ferrite-to-ferrite grain boundaries, we use a red dashed line as marker. To overcome these problems, we apply several morphological operations, which are described step-by-step in the sequel and are illustrated in Fig. 5.

Fig. 5 a *Grayscale* image-quality map corresponding to the *blue frame* marked in Fig. 4a with the size of $5\,\mu\text{m} \times 5\,\mu\text{m}$. **b** Reconstruction of ferrite (*white*) and martensite (*black*) phase by the application of the threshold $Z_{Q_{\text{normal}}}$ determined by the intersection point in Fig. 4b. Additionally the unsafe regions are marked: holes (*green solid lines*), thin structures (*red dotted lines*). Resulting phase reconstructions after applying image processing steps in the following order: **c** filling small regions, originally identified as ferrite, **d** double staggered erosion of the martensite phase by a 3×3 sample, **e** double staggered dilatation of the martensite phase by a 3×3 sample. **f** Color map of the differences between the original (**b**) and filtered (**e**) phase reconstruction, where removed and added pixels are colored *red* and *green*, respectively. (Colour figure online)

We start with a simple "filling small regions" operation on the binary image of the phase reconstruction, whereby all ferrite regions with an area surface lower than 75 pixels are switched to martensite, cf. Fig. 5c. To remove the pixels associated with thin structures like the ferrite-to-ferrite grain boundaries, we apply a two-stage procedure. In the first stage we use a double staggered erosion of the black (martensite) pixel. In each erosion step a 3×3 sample consisting of white pixel is placed centered on each white pixel, whereby neighboring
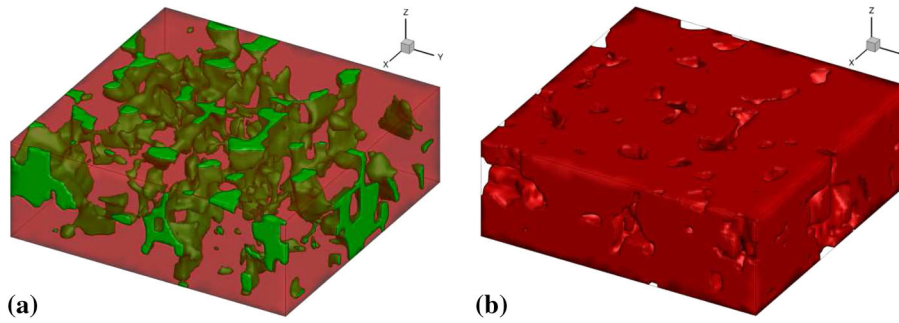
Fig. 6 Reconstruction of microstructure obtained from *Slicescan 1*: **a** full phase representation (*red* ferrite, *green* martensite), **b** ferrite phase. The dimensions are 15.9 μm × 16.45 μm × 5 μm. (Colour figure online)

black (martensite) pixels are overwritten. Doing this in a double- staggered procedure, thin structures up to 4 pixel in width and height can be removed. This is a typical size of the grain boundaries appearing in the structures analyzed here. Obviously, in addition to the grain boundaries the size of the martensite inclusions is decreased by this erosion process, cf. Fig. 5d. To correct for this effect, we apply the counterpart of the erosion procedure, a double staggered dilation, thereafter. On that account, a 3 × 3 sample consisting of black pixels is placed centering on each black pixel in two cycles, where the result is shown in Fig. 5e. The reason for the double staggering for both steps is that a direct application of an, e.g., 5 × 5 sample will produce a coarsening of the curved shape of the martensite islands. The effects of the described boolean operations are shown by a color indication of the differences between the initial phase reconstruction (Fig. 5b) and the resulting cleaned phase reconstruction (Fig. 5e) in Fig. 5f. Therein the (martensite) pixels added by the "filling small region" operation are colored green and the (martensite) pixels removed by the "erosion" operations are colored red. A direct comparison with the original grayscale image-quality map (Fig. 5a) shows the functionality of the applied method.

At this point one side effect of the "erosion–dilation" operation should be mentioned. The sharp and spike-like boundaries of the martensite inclusions in the initial phase reconstruction are smoothed, which is helpful for later discretization by finite elements, but it is disadvantageous for a precise reconstruction. Note that for higher-order computational modeling approaches, where specific material properties are assigned even to the ferritic grain boundaries or where the individual character of grains have to be taken into account in case of crystal plasticity FE-approaches, the thin lines may be treated differently in order to specifically identify these grain boundaries.

3.2 Results for DP steel microstructures

The previously presented procedure is applied to the data sets obtained by the EBSD measurements mentioned in Sect. 2 for the phase reconstruction of the DP steel's microstructure. All datasets consist of compilations of microstructural information determined by in-plane measurements on small areas. The phase reconstruction method is individually applied to each of these in-plane data sets, i.e., (i) the histogram is computed, (ii) the threshold $Z_{Q_{normal}}$ is determined, (iii) the phases are reconstructed, and (iv) the filters are applied.

Between each measurement for *Slicescan 1* and *Slicescan 2* the position difference can be described as a vector orthogonal to the measured area, i.e., in the transverse direction (TD), see Fig. 2. Consequently, from these data sets a three-dimensional phase reconstruction of the microstructure can be obtained by stacking the slices. Here we use the software Mimics®[1] to generate a three-dimensional geometrical model. The resulting phase reconstructions for *Slicescan 1* and *Slicescan 2* are visualized in Figs. 6 and 7, respectively.

In contrast, the measurement of the *Largescan* produces datasets whose offset vectors lie in the same plane as the measured area, i.e., RD–ND plane, see Fig. 2. Consequently, the application of the phase reconstruction method results in 132 two-dimensional phase reconstructions. In Fig. 8 the complete grayscale image-quality map and the resulting phase reconstruction is shown. Note that in order to reduce the size in this visualization, we omit the distance between the representation of the individual small area scans, cf. Fig. 3, and place the areas directly next to each other.

---

[1] Medical Image Segmentation for Engineering on Anatomy™ (Mimics®) is a registered trademark of the Materialise HQ, Belgium.
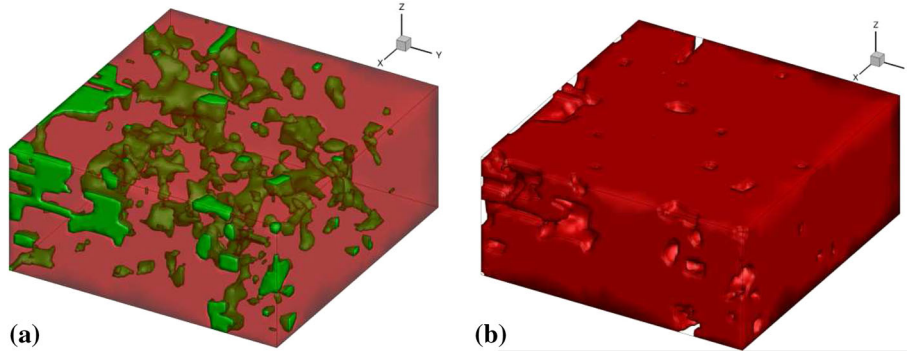
Fig. 7 Reconstruction of microstructure obtained from *Slicescan 2*: **a** full phase representation (*red* ferrite, *green* martensite), **b** ferrite phase. The dimensions are 21.6 μm × 20.78 μm × 9.7 μm. (Colour figure online)
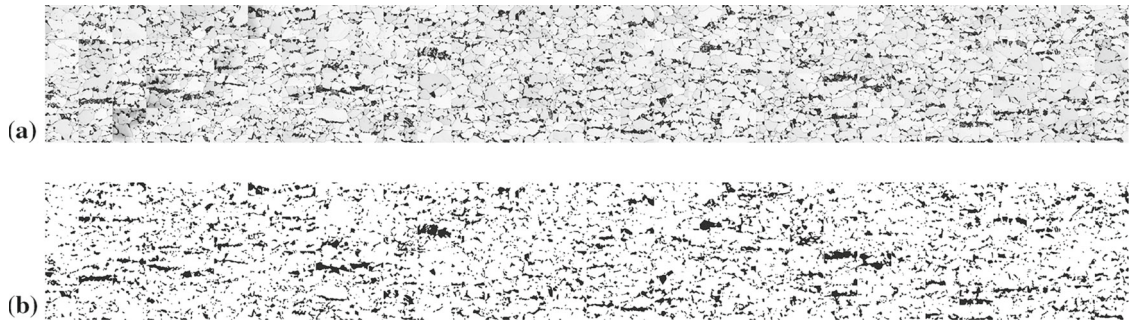
Fig. 8 Reconstruction of the Largescan measurement: **a** grayscale image-quality map and **b** filtered phase reconstruction (ferrite: *white*, martensite: *black*). The dimensions of the total area are 15.98 mm × 1.56mm (including large step size) and for each block 15 μm × 15 μm

4 Representativity of 3D reconstructions

The choice of the representative volume element (RVE) is a crucial part of the homogenization of random microstructures. A suitable RVE should represent the characteristics of the microstructure morphology to serve as basis for a reliable computation. For the characterization of the morphology several statistical measures have been introduced in the literature. For a general discussion see e.g., [10,59] and [47]. Various statistical descriptors have been introduced in the last decades, see. e.g., [27,103], or [91] for comprehensive overviews. Such descriptors can be divided into scalar-valued quantities like, e.g., some basic parameters such as the volume fraction or the internal surface density, and statistical measures of higher order.

For our analysis we focus on the scalar-valued basic parameters as statistical descriptors of the morphology of the considered DP steel. First we determine these statistical quantities of the two-dimensional reconstructions obtained from the *Largescan* measurement. They should serve as reference since [21] have shown that the large scan area is a reliable technique to measure characteristics of multiphase materials, e.g., the phase fraction. After that we compute and compare the statistical values for the two three-dimensional reconstructions to analyze their representativity.

4.1 Basic parameters

For the statistical description of random microstructures basic parameters can be analyzed, cf. [59]. Since we here focus on a DP steel, which typically consists of two phases, i.e., ferrite and martensite, we introduce these parameters for the martensite inclusion phase.

The first essential parameter is the phase fraction, which is defined as the volume fraction of the inclusion phase in the three-dimensional case and as the cross-sectional area fraction in the two-dimensional case, i.e.,

$$\mathcal{P}_V := \frac{V^{\mathrm{I}}}{V^0} \quad \text{and} \quad \mathcal{P}_A := \frac{A^{\mathrm{I}}}{A^0}, \tag{3}$$

where V denotes the volume and A the cross-sectional area. For an estimation of the volume fraction based on the two-dimensional data the relation $\mathcal{P}_V^* = \mathcal{P}_A$ is used. The superscripts I and 0 indicate the quantities computed for the inclusion phase and the total microstructure, respectively. Thus, for example V^{I} denotes the volume of the inclusion phase and V^0 is the total volume. While these fractions describe how the inclusion phase assemble the whole microstructure, the specific internal surface density is a measure for how fine the inclusion phase is distributed. In the three-dimensional case it can be calculated by

$$\mathcal{P}_S := \frac{S^{\mathrm{I}}}{V^{\mathrm{I}}} \tag{4}$$

with the interface area S^{I} separating the inclusion and matrix phase. Its counterpart for a two-dimensional cross section is the specific internal interface length density

$$\mathcal{P}_L := \frac{L^{\mathrm{I}}}{A^{\mathrm{I}}} \,, \tag{5}$$

where L^{I} describes the circumference of the inclusions in the considered cross section. Both quantities can be related to each other following [59] such that a three-dimensional measure $\mathcal{P}_S$ can be estimated in terms of the 2D counterpart $\mathcal{P}_L$ by $\mathcal{P}_S^* = 4\,\mathcal{P}_L/\pi$. This relation is important for later analysis of the reconstructions, since statistics obtained from the reconstructions of the two-dimensional *Largescan* dataset will be compared with the ones of the three-dimensional data sets *Slicescan 1* and *Slicescan 2*. The characteristics of the shape of the inclusion, e.g., convexity or non-convexity, can be captured by the specific density of the integral of the mean curvature, i.e.,

$$\mathcal{P}_M := \frac{M^{\mathrm{I}}}{V^{\mathrm{I}}} \,, \tag{6}$$

where V^{I} denotes the volume of the inclusion. In this equation the integral of the mean curvature M^{I} over the interface S between inclusion and matrix is considered, where the definition is

$$M^{\mathrm{I}} := \frac{1}{2} \int_S \left(\min_\beta[\kappa] + \max_\beta[\kappa] \right) \mathrm{d}S. \tag{7}$$

Herein κ is the curvature in a certain tangential direction β defined as $\kappa(\beta) := 1/r(\beta)$ with the curvature radius r. For the following statistical analysis we use the relation $\mathcal{P}_M^* = 2\pi X_A$ with the specific Euler number X_A following [59] to compare the values for the two- and three-dimensional reconstructions.

4.2 Statistical analysis

The evaluation of the representativity of the reconstructed three-dimensional microstructures is conducted by a statistical analysis using the basic parameters from Sect. 4.1. Following [21] we use the quantities obtained from the *Largescan* as reference values. For the correlation of the two-dimensional and three-dimensional quantities we assume that the ensemble average of the cross-sectional area fraction $\overline{\mathcal{P}}_V^*$, computed for each block in *Largescan*, is statistically comparable to the volume fraction $\mathcal{P}_V$ of the volumetric structures, which is identical to the phase fraction. For the 3D counterparts of the phase fraction, the specific internal surface density, and the specific density of the integral of the mean curvature, we use the relations given in Sect. 4.1 for the correlation between the two- and three-dimensional case. For the quantities computed from the *Largescan* data, we calculate the ensemble average over all individual small area scans, i.e., for a particular quantity $\mathcal{P}_Q$ the ensemble average is calculated by

$$\overline{\mathcal{P}}_Q^* := \frac{1}{n_{\mathrm{blocks}}} \sum_{i=1}^{n_{\mathrm{blocks}}} \mathcal{P}_{Q,i}^* \quad \text{with} \quad Q = V, S, M, \tag{8}$$

where n_{blocks} denotes the number of small area scans in the *Largescan*. For the numerical calculation of the basic parameters the algorithms provided by [59] are used.

In Fig. 9 the distribution of the basic parameters over the small area scans obtained from the *Largescan* is shown ($\cdots$). Using Eq. (8) the ensemble average $\overline{\mathcal{P}}_V^*$ ($\cdots$) and the standard deviation (■) is calculated and
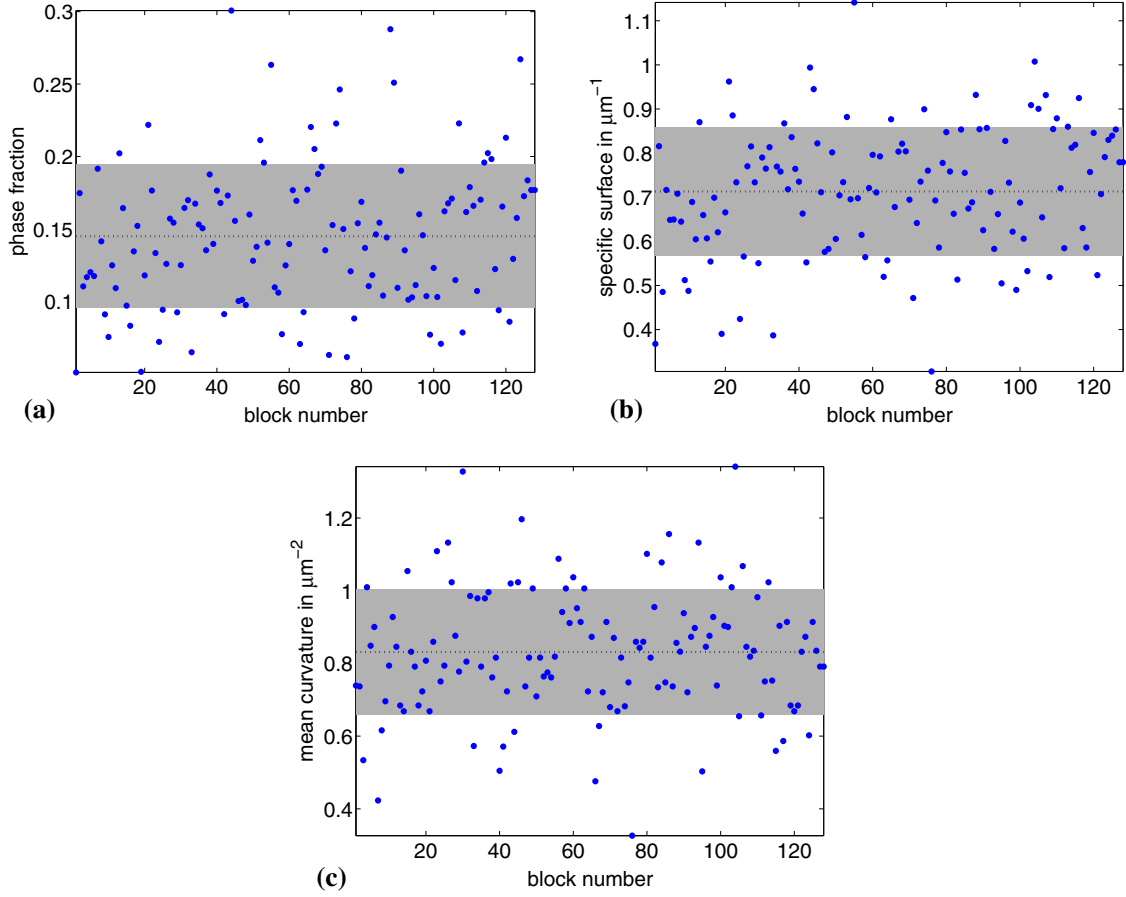
Fig. 9 Basic parameters of *Largescan*: **a** phase/cross-section area fraction $\mathcal{P}_V^*$, **b** specific internal surface density $\mathcal{P}_S^*$ and **c** specific density of the integral of the mean curvature $\mathcal{P}_M^*$. Statistical measures evaluated for each block (*blue dots*), ensemble average (*dotted line*) and standard deviation (*gray square*). (Colour figure online)

Table 2 Basic parameters computed for the reconstructions described in Sect. 3.2

	Largescan			*Slicescan 1*		*Slicescan 2*	
	Value	Std.dev. (%)		Value	Error (%)	Value	Error (%)
$\overline{\mathcal{P}}_V^*$	0.144	±34.38	$\mathcal{P}_V$	0.099	−31.25	0.089	−38.19
$\overline{\mathcal{P}}_S^*$	0.713	±20.34	$\mathcal{P}_S$	0.645	−9.54	0.612	−14.17
$\overline{\mathcal{P}}_M^*$	0.831	±20.70	$\mathcal{P}_M$	1.071	28.88	0.976	17.45

The values for *Largescan* are ensemble averages over the whole set of small area scans, whereby the values for *Slicescan 1* and *Slicescan 2* are directly computed from the three-dimensional representation

also plotted. It can be seen that the values of the parameters calculated for some small areas are out of the range of the standard deviation. This shows that a single small area cannot be considered as representative and substantiates the application of the large area scan technique. For the reconstructions of *Slicescan 1* and *Slicescan 2* we also compute the statistical parameters and summarize all results in Table 2, where we also add the relative deviation with respect to the *Largescan* data set.

The comparison of the basic parameters computed for the slicescans with the ones of the *Largescan* in Table 2 shows the poor representativity of the full reconstructions of *Slicescan 1* and *Slicescan 2*. The values differ significantly from the reference and the deviation is close to the standard deviation in some cases. At first glance this could be unexpected, because the values of the measurements of the cross sections (slicescans) are a kind of averages over several two-dimensional data comparable to the ensemble averages computed from the measurements of the large specimen (*Largescan*). But the measurements for the slicescans are scanned only

with a small step size (0.1 μm) in the third direction to get smooth reconstructions of the inclusions' geometry. Consequently, the variance of the measurement position in the material is much smaller than during the large area scan technique, where the area-to-area distance is approximately 500 μm, cf Sect. 2. This enhances the representativity of the measurement, cf. [21,22]. An obvious solution may be to increase the measurement region, but the investigated volumes is still technically limited in size by the measurement technique. A higher representativity may be obtained by choosing a more suitable position for the EBSD measurements within the sample. However, this is difficult due to the high complexity associated with the underlying measurement technique.

4.3 Mechanical comparison

For completeness we compute the overall mechanical response of the reconstructed microstructures for uniaxial tension and compare them with experimental data, which was provided by ThyssenKrupp Steel Europe. For this purpose first the framework for the numerical calculations is briefly recapitulated.

4.3.1 Computational modeling

For the numerical computations we use direct two-scale finite element simulations to obtain the overall effective mechanical behavior. On that account we give here only a briefly recapitulation of this approach and for details we refer to, e.g., [28,56,74,75,82]. In computational homogenization a RVE representing the underlying microstructure is attached at each integration point of the discretized macroscopic boundary value problem. Consequently, at the microscale, additional boundary value problems have to be solved where the deformations are described in terms of the microscopic deformation gradient F with $J := \det[F] > 0$. With the associated work-conjugated stress measure, the first Piola–Kirchhoff stress tensor P, the microscopic Cauchy stresses are computed by $\sigma = \frac{1}{J} P F^{\mathrm{T}}$. Overlined characters are related to the macroscopic level as, e.g., the macroscopic deformation gradient $\overline{F}$ with $\overline{J} := \det \overline{F} > 0$ and the first Piola–Kirchhoff stress tensor $\overline{P}$. The latter quantity can be calculated by volumetric averaging, i.e.,

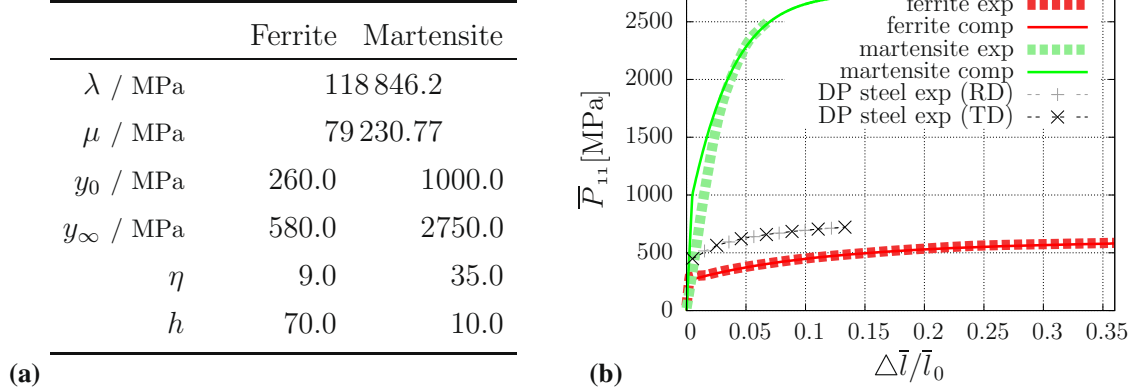$$\overline{P} = \frac{1}{V} \int_{\mathcal{B}} P \, dV \quad \rightarrow \quad \overline{\sigma} = \frac{1}{\overline{J}} \overline{P} \, \overline{F}^{\mathrm{T}} ; \tag{9}$$

the domain of the RVE with volume V is denoted by $\mathcal{B}$. From the macro-homogeneity condition also referred to as Hill–Mandel condition, see [34], suitable boundary conditions at the microscale are derived. Well-known boundary conditions fulfilling this condition are (i) the uniform traction conditions, (ii) the linear displacement conditions, and the (iii) periodic boundary conditions. In this paper linear displacement boundary conditions and periodic boundary conditions are applied depending on the periodic or non-periodic morphology of the microstructure. The consistent macroscopic moduli are considered for higher computational efficiency, for details we refer to [55] and [75], in this context see also [89].

Since in the simulations the different constituents of the DP steel microstructure are resolved, i.e., ferrite and martensite, an isotropic finite elastoplasticity formulation for the individual phases at the microscale is needed. Here, a standard isotropic finite J_2 elastoplasticity formulation is considered which is based on the multiplicative decomposition of the deformation gradient $F = F^{\mathrm{e}} F^{\mathrm{p}}$ in an elastic (F^{e}) and a plastic part (F^{p}), see [46,48]. For details of the thermodynamic formulation as well as for the numerical treatment see [43,53,54,66,79–81]. The strain energy function is assumed to be additively decoupled into an elastic part and a plastic part. Following [80] a quadratic elastic free energy function in terms of the logarithmic elastic strains is considered making use of the Lamé parameters λ and μ. For the plastic behavior the individual phases are assumed to follow an exponential-type hardening as in [94], superimposed with a linear hardening. Thus, the plastic strain energy function reads

$$\psi^{\mathrm{p}} = y_{\infty}\alpha - \frac{1}{\eta}(y_0 - y_{\infty}) \exp(-\eta\alpha) + \frac{1}{2} h \, \alpha^2 \tag{10}$$

with the equivalent plastic strains α. The associated hardening function $\beta = \partial_{\alpha} \psi^{\mathrm{p}}$ fits appropriately experimental yield curves of purely ferritic and purely martensitic steels. The material parameters y_0, y_{∞}, η and h are the initial yield strength, the plastic yield strength at the initialization of the linear hardening, the degree of exponential hardening, and the slope of superimposed linear hardening, respectively. The flow rule for the

	Ferrite	Martensite
λ / MPa	118 846.2	
μ / MPa	79 230.77	
y_0 / MPa	260.0	1000.0
y_∞ / MPa	580.0	2750.0
η	9.0	35.0
h	70.0	10.0

(a)

(b)

Fig. 10 a Material parameters adjusted to experimental curves, **b** nominal stresses $\overline{P}_{11}$ in MPa versus strains $\Delta\overline{l}/\overline{l}_0$ in uniaxial tension (loading direction: RD) for the experimental data (courtesy of ThyssenKrupp Steel Europe) and the resulting model response: pure ferrite which is produced in the laboratory adjusting for a similar alloying composition as in the ferrite of the DP steel, pure martensite (produced in laboratory) adjusting for a similar carbon content as in the martensite in the DP steel, and experimental response in RD- and TD-direction of the considered DP steel

plastic quantity is integrated using an implicit exponential update algorithm, which preserves plastic incompressibility [43,54,80,95].

For the elastic response in the individual phases, it is assumed that both phases behave like the overall DP steel and an elasticity modulus of $E = 206,000$ MPa and a Poisson ratio of $\nu = 0.3$ are identified from experiments. The associated Lamé-parameters are $\lambda = 118,846.2$ MPa and $\mu = 79,230.77$ MPa. For the characterization of the hardening behavior, uniaxial tension tests are performed for the single phases and then the finite plasticity model as described above is adjusted to the experiments. For this purpose, artificial pure ferrite and martensite materials need to be produced in the laboratory which exhibit the similar alloying element composition, grain size distribution and thus a similar material behavior compared to the individual phase materials of the DP steel. This may influence the quality of direct micro–macro calculation of DP steels compared with macroscopic experimental data. In particular this is not straightforward at all for the pure ferrite material such that still a significant deviation may occur with respect to the ferrite for the DP steel. The associated stress–strain response for the individual phases obtained from experiments and from computations using the elastoplasticity formulation are illustrated in Fig. 10b and the associated material parameters are given in Fig. 10a. The production poses extraordinary challenges to the experimentalist since the artificially produced pure phases differ from the phases occurring in the micro-heterogeneous DP steel. The crucial part in the production of the pure martensite specimen is represented by the carbon content, since in DP steels the martensite inclusions tend to attract more carbon during the production process and show therefore a higher carbon content than the pure material artificially produced with the same alloying elements. Consequently, an artificially produced pure martensite with an increased carbon content of approximately 50% is investigated. It is remarked that in DP steels the martensite undergoes mainly elastic deformations since the initial yield stress is significantly higher than the one of ferrite and thus, the plastic yielding regime is typically not reached in the martensite. Additionally, [33] showed, that during the production of pure martensitic steel different martensite blocks are formed, which reveal different nanohardnesses. But here we are only interested in the overall mechanical behavior of the martensite and not in particular martensite blocks. Consequently, the aforementioned issue of varying mechanical properties through the martensite phase is of lower relevance and is not considered in the following. For comparison, the computational microstructure models with the real material response we take into account data from experiments provided by ThyssenKrupp Steel Europe. These experiments consider uniaxial tension applied to a test specimen, which is manufactured from the DP steel by cutting a strip along the rolling direction (RD) and the transverse direction (TD) of the sheet. The overall mechanical response of the DP steel is also depicted in Fig. 10b which shows similar curves for the RD- and the TD-directions.

4.3.2 Reconstructed three-dimensional microstructures

For the numerical computation using the two-scale finite element simulation we discretize the reconstructions of *Slicescan 1* and *Slicescan 2* by 10-noded tetrahedral finite elements. The mesh constructions were
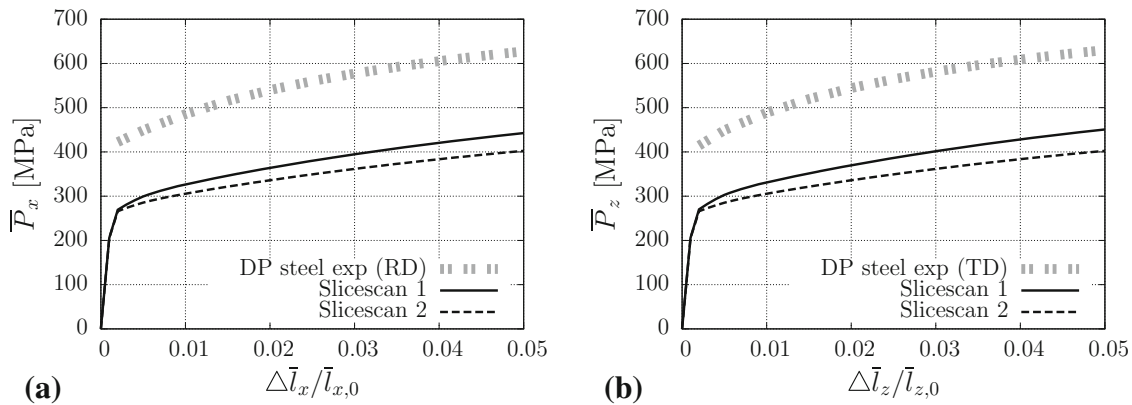
Fig. 11 Overall mechanical response, i.e., first Piola– Kirchhof stresses versus relative elongation, from uniaxial tension tests of the considered DP steel and the reconstructions of *Slicescan 1* and *Slicescan 2*. **a** RD-direction ($\overline{P}_x$ vs. $\triangle\overline{l}_x/\overline{l}_{x,0}$), **b** TD-direction ($\overline{P}_z$ vs. $\triangle\overline{l}_z/\overline{l}_{z,0}$). The experimental curves are provided by ThyssenKrupp Steel Europe

done in the software package 3-matic®[2] because of its direct interface for the import of the geometrical data obtained with Mimics[TM], cf. Sect. 3.2. The discretization results in 612.323 and 413.681 finite elements for the microstructure of *Slicescan 1* and *Slicescan 2*, respectively. Since the morphology of the microstructures is not periodic at the boundary, we apply linear displacement boundary conditions at the microscale.

In Fig. 11 the comparison of the overall mechanical response of the real material in the uniaxial tension experiments and the results obtained from the simulations of the three-dimensional microstructures are shown. A rather big gap between simulations and experiment is observed. A possible reason is that the martensite phase fraction is too small, which was already identified in Sect. 4.2. Since martensite has a higher yield curve, a higher yield curve of the calculation for the DP steel would be expected for larger martensite fractions as well. As will be seen later in this paper, this, however, is not the main reason. Consequently, the reconstructed three-dimensional microstructures hardly serve as RVEs in, e.g., homogenization procedures of multiscale simulations. In the sequel an approach to overcome this problem is presented in order to achieve an RVE for the computation of the overall effective mechanical properties of the considered DP steel.

5 SSVEs for the simulation of dual-phase steels

From the statistical analysis shown in the Sect. 4.2, we summarize that the full reconstruction of the three-dimensional microstructure cannot be used in a straightforward way to devise RVEs for the computation of the overall effective mechanical properties. The challenge associated with these reconstructions is given by the technical limitations associated with the measurement technique, namely, an insufficient size of the reconstructed portion leading to an inclusion morphology, which statistically differs from the reference. Due to relatively high efforts associated with the EBSD–FIB measurement, it cannot be expected that a specific microstructure can be measured which shows exactly representative properties. Consequently, the first natural concept to fix this, is a suitable modification of the geometrical representation of the inclusion morphology. For instance, the inclusion morphology may be modified such that the martensite phase fraction of the 3D microstructure matches closely the reference. This is, however, not a trivial step for reproducing the real microstructures due to their complex geometrical morphology. On that account we decide to construct statistically similar volume elements (SSVEs) based on the three-dimensional microstructures, which are characterized by a lower complexity compared to the real microstructures but which represent the overall material behavior well. These SSVEs may then serve as microstructures which may be more conveniently modified. Additionally, one aim of this paper is to achieve an RVE for efficient two-scale finite element simulations. In general the number of degrees of freedom of such SSVEs, which leads to a more efficient scheme, see [9], is significantly lower.

---

[2] 3-matic®is a registered trademark of the Materialise HQ, Belgium

Table 3 Results of the SSVE construction process based on volume fraction, spectral density and lineal-path function—values of objective function $\mathcal{E}$, and individual least-square functionals, number of tetrahedral elements n_{ele} and mechanical errors $\tilde{r}$ in % for the individual SSVEs shown in Fig. 12a, b

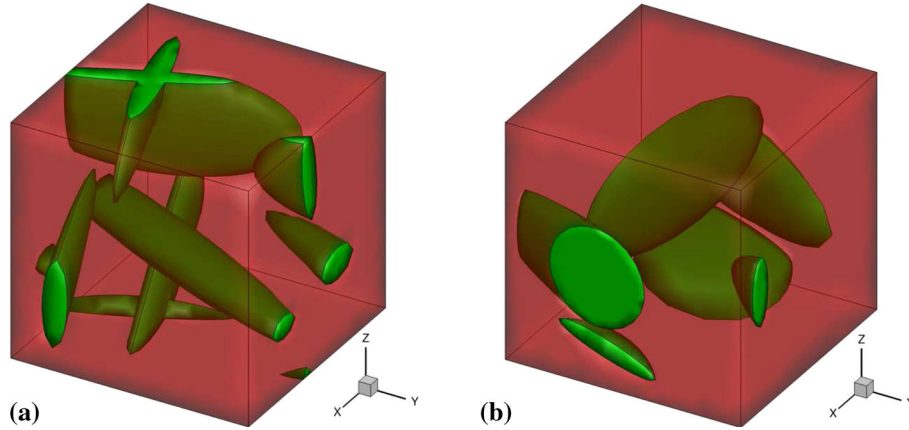|	$\mathcal{E}/\ 10^{-2}$	$\mathcal{L}_{\mathrm{V}}/\ 10^{-4}$	$\mathcal{L}_{\mathrm{SD}}/\ 10^{-3}$	$\mathcal{L}_{\mathrm{LP}}/\ 10^{-4}$	n_{ele}	$\tilde{r}_x$	$\tilde{r}_z$	$\tilde{r}_{xy}$	$\tilde{r}_{yx}$	$\tilde{r}_{\varnothing}$
SSVE 1	0.53	3.37	3.3	0.017	15,714	0.2	2.4	1.2	1.1	1.45
SSVE 2	0.86	21.4	2.28	0.042	16,000	3.49	3.67	0.63	0.76	2.58

Table 4 Basic parameters computed for the *Largescan* and the SSVEs constructed from the *Slicescan 1* and *Slicescan 2*

	Largescan			SSVE 1		SSVE 2	
	Value	Std.dev. (%)		Value	Error (%)	Value	Error (%)
$\overline{\mathcal{P}}_V^*$	0.144	±34.38	$\mathcal{P}_V$	0.097	−32.64	0.092	−36.11
$\overline{\mathcal{P}}_S^*$	0.713	±20.34	$\mathcal{P}_S$	0.622	−12.76	0.839	17.67
$\overline{\mathcal{P}}_M^*$	0.831	±20.70	$\mathcal{P}_M$	0.731	−12.03	1.325	59.45

5.1 Construction of SSVEs

The construction method was originally introduced for two-dimensional microstructures, cf. [6], and referred to as statistically similar *representative* volume element (SSRVE). In Sect. 4.3.2 it is shown, that the reconstructed real microstructure turned out to be not necessarily representative with respect to the reference, i.e., experimental data of the DP steel. Based on that a similar behavior is expected for the constructed and non-modified SSVEs. Consequently, we omit *representative* in the notation of these volume elements as well as the R in the corresponding abbreviation. Here, we briefly summarize the method and give several references for detail studies. For the construction of three-dimensional SSVEs representing the reconstructions of *Slicescan 1* and *Slicescan 2* we follow the strategy presented by [9]. They propose the usage of phase fraction, spectral density, and lineal-path function as suitable statistical measures for the characterization of the microstructure morphology. The spectral density is related to the periodicity eventually hidden in the microstructure. The lineal-path function characterizes the geometrical shape of inclusions. The differences of these statistical measures calculated for the real microstructure and the SSVE are used to define suitable least-square functionals. These functionals build an objective function, which is minimized during the construction process. Since in [9] it turns out that an inclusion morphology of the SSVEs assembled by three ellipsoids obtains good results for DP steel microstructures, we choose this parametrization of the SSVE. Consequently, the size, position and orientation of the ellipsoids represent the degrees of freedom for the optimization problem. It should be also mentioned that the assembly of the ellipsoids is done such that periodic structures are achieved. Consequently, in the numerical simulation periodic boundary conditions can be applied. Further studies and information regarding the construction of SSRVE can be also found for the two-dimensional case in, e.g., [4,7,8]. On the construction of three-dimensional SSRVEs using Minkowski Functionals as statistical descriptors we refer to [73].

In Table 3 results of the SSVE construction process are summarized giving the final value of the minimized objective function $\mathcal{E}$, the least-square functionals of the statistical measures and the mechanical error obtained in four virtual experiments. The objective function and the least-square functionals $\mathcal{L}$ are formulated following [9] which are based on the martensite volume fraction ($\mathcal{L}_{\mathrm{V}}$), the spectral density ($\mathcal{L}_{\mathrm{SD}}$) and the lineal-path function ($\mathcal{L}_{\mathrm{LP}}$). The least-square functionals take into account the deviation of the statistical measure computed from the constructed SSVE and the statistical measure characterizing the real microstructure, for details see [8,9]. The overall mechanical error $\tilde{r}_{\varnothing}$ is computed as average of the four virtual experiments, i.e., uniaxial tension in horizontal and vertical direction in the RD–TD plane with free lateral conditions ($\tilde{r}_x$ and $\tilde{r}_z$, respectively) and two simple shear tests where the RD-ND plane is shifted in RD-direction and ND-direction ($\tilde{r}_{xy}$ and $\tilde{r}_{yx}$, respectively). From the values of the objective function and the mechanical errors, it can be seen that the SSVE 1 is statistically as well as mechanically more similar to its target structure *Slicescan 1* than SSVE 2 to its target structure *Slicescan 2*. But due to the larger numerical effort characterized by the larger number of finite elements needed for the discretizations of the real microstructures (up to 38 times more finite elements than the SSVEs), the obtained representation by SSVEs is considered as sufficiently accurate.

Fig. 12 **a** SSVE 1 associated with *Slicescan 1* and **b** SSVE 2 associated with *Slicescan 2*

Table 5 Values of objective function $\mathcal{E}$, and individual least-square functionals and number of tetrahedral elements n_{ele} determined for the SSMVEs

	$\mathcal{E}/\ 10^{-2}$	$\mathcal{L}_{V}/\ 10^{-4}$	$\mathcal{L}_{SD}/\ 10^{-3}$	$\mathcal{L}_{LP}/\ 10^{-4}$	n_{ele}
SSMVE 1	115.2	2088.2	3.3	9.39	24,749
SSMVE 2	127.33	2422.6	2.09	10.29	31,491

Table 6 Basic parameters computed for the *Largescan* and SSMVEs

	Largescan			SSMVE 1		SSMVE 2	
	Value	Std.dev. (%)		Value	Error (%)	Value	Error (%)
$\overline{\mathcal{P}}_{V}^{*}$	0.144	±34.38	$\mathcal{P}_{V}$	0.144	0.0	0.144	0.0
$\overline{\mathcal{P}}_{S}^{*}$	0.713	±20.34	$\mathcal{P}_{S}$	0.788	10.52	0.958	34.36
$\overline{\mathcal{P}}_{M}^{*}$	0.831	±20.70	$\mathcal{P}_{M}$	0.726	−12.64	0.600	−27.80

In Fig. 12, the constructed SSVE 1 and SSVE 2 associated with the reconstruction of *Slicescan 1* and *Slicescan 2* respectively, are visualized. The discretization of the SSVEs are also used to simulate the uniaxial tension tests in RD- and TD-directions according to the available experimental results. In Table 4 the basic parameters of the SSVEs are compared with the reference values obtained from the *Largescan*. As expected the error is comparable with the real 3D microstructures *Slicescan 1* and *Slicescan 2*.

5.2 Modification of the phase fraction

For the modification of the martensite phase fraction in the SSVEs, we take advantage of their parametrization used for the construction. Therein the size of the ellipsoids is characterized by the radii of the three semi-axes. Consequently, we scale all the radii up in an iterative manner until the phase fraction of the reference, i.e., 14.4%, is reached, cf. Table 2. The resulting statistically similar modified volume elements are referred to as SSMVE 1 and SSMVE 2, where the factors applied to the original radii are 1.14 and 1.13, respectively.

The values of the objective function are given in Table 5. Since just the size of the inclusions, not their shape, is modified, the similarity of statistical measures apart from the phase fraction is reduced, as can be seen by comparing $\mathcal{E}$ in Table 5 with the ones given in Table 3 for the SSVEs.

To make sure, that the modifications do not change the statistical properties of the SSVE with respect to the reference, we also calculate the basic parameters of the SSMVEs, see Table 6. For the allowed deviation of the values, we use again the standard deviation obtained from the statistical analysis of the *Largescan* given in Table 2.

The effective mechanical responses in the uniaxial loading situations are plotted in Fig. 13. As expected an increase of both stress levels of the SSMVEs due to the modification can be observed. Although the phase
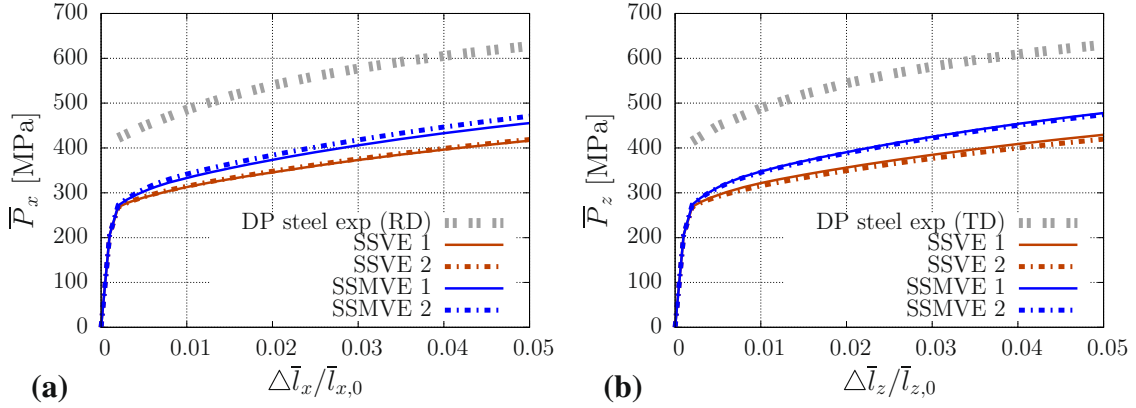
Fig. 13 Overall mechanical response, i.e., first Piola– Kirchhoff stresses versus relative elongation, from uniaxial tension tests of the considered DP steel, the original SSVEs and the volume-modified SSMVEs. **a** RD-direction ($\overline{P}_x$ vs. $\triangle\overline{l}_x/\overline{l}_{x,0}$), **b** TD-direction ($\overline{P}_z$ vs. $\triangle\overline{l}_z/\overline{l}_{z,0}$). The experimental curves are provided by ThyssenKrupp Steel Europe
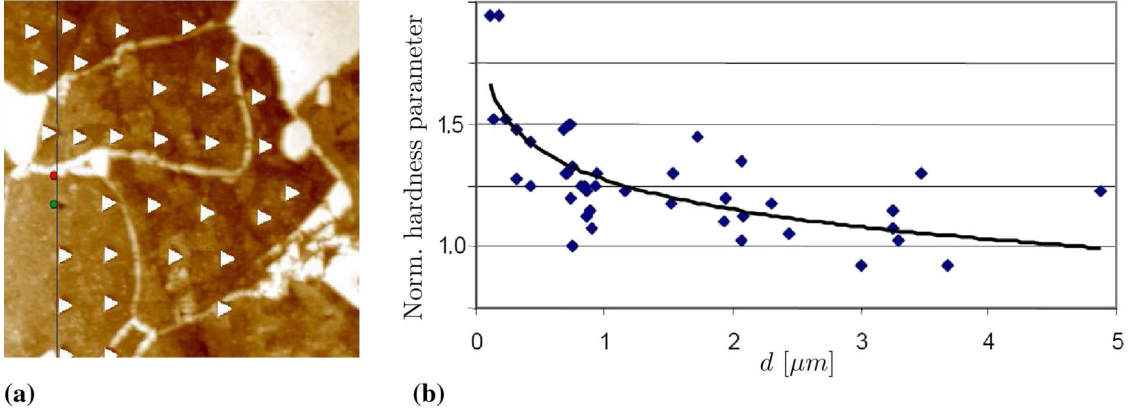
Fig. 14 **a** An illustration of characteristic nanoindentation measurement positions and **b** normalized hardness parameter (normalized with respect to the value in the ferrite at a far distance from the martensite inclusions) versus distance d from the inclusions obtained by nanoindentation tests performed at ThyssenKrupp Steel Europe (Taken from [77])

fraction is an essential aspect in the framework of RVE construction the resulting stress–strain response is still far away from the experimental results. Consequently, some physics at the microscale are not captured by the numerical approach so far.

5.3 Initial volumetric strain approach

During the production process of DP steels, the martensite inclusions arise from a transformation of austenite to martensite induced by rapid cooling. The difference in the specific volumes of austenite and martensite leads to a volume expansion of approximately 4 % of the inclusion phase relative to the surrounding ferrite matrix, cf. [57,61,71]. This mechanism induces an initial pre-straining and hence some degree of hardening at the microscale, especially on DP steels see [38].

In order to obtain information regarding such distributed zones of initial hardening, nanoindentation tests were performed at ThyssenKrupp Steel Europe at different microscopic positions, see [77], cf. also Fig. 14a. The hardness is measured and plotted versus the distance from the martensite inclusions in Fig. 14b. It can be clearly seen that the associated regression curve shows an exponential-type decrease of hardness in the ferrite phase with an increasing distance from the inclusions. The hardness is approximately 1.6 times higher close to the inclusion than in the ferrite far away from the inclusion. These distributed properties are expected to result from carbon diffusion as well as an accumulation of dislocations which are in turn due to the austenite martensite phase transformation. Since the hardness correlates with the initial yield stress the typical assumption of a

homogeneous material behavior in the ferrite matrix appears not to be valid, see e.g., [67]. It is rather required to consider a distributed yield behavior in the ferrite.

On that account we apply a two-step approach, cf. first ideas in [77]. The first step includes an application of an initial volumetric strain by a virtual temperature expansion in the martensite phase, which is also applied by [64]. This step is motivated by the volume change during the production process which yields the initial hardening as well as associated microscopic eigenstresses. Afterward a locally distributed modification of the ferrite yield law correlated with the arising equivalent plastic strain distribution is done. Thereby, it is assumed that the microscopic distribution of ferrite yield properties is qualitatively similar to the plastic strains associated with the initial hardening. Motivated by the different yield behavior in the neighborhood of the martensite inclusions, [76] proposed an interzone around these inclusions with modified yield criteria. Also [38] modeled distributed mechanical properties by several layers with varying material parameters around the martensite inclusions.

5.3.1 Application of initial volumetric strains (IVS)

It is to be expected that the initial hardening zones are caused by the volumetric jump in the inclusions when transforming from austenite to martensite. Thus, it is reasonable to apply numerically volumetric strains in the inclusions in order to account for distributed hardening in the externally unloaded situation. In the following the procedure for incorporating such volumetric strains in close association with a virtual temperature expansion is explained.

Let us consider the thermoelastic potential in terms of the elastic left Cauchy–Green tensor $\boldsymbol{b}^e = \boldsymbol{F}^e \boldsymbol{F}^{eT}$ and the temperature change ϑ

$$\psi = \psi^{vol}(J_e) + \psi^{iso}(\boldsymbol{b}^e) + H(\vartheta), \tag{11}$$

where the volumetric and isochoric elastic potentials are denoted by ψ^{vol} and ψ^{iso}, respectively, and H is a thermal part. Following the Duhamel–Neumann hypothesis for isothermal expansion, we consider the multiplicative decomposition of the determinant of $\boldsymbol{F}$

$$J = \det \boldsymbol{F}, \quad J = J_e J_\vartheta \quad \text{with} \quad J_\vartheta = e^{3\alpha_T \vartheta}. \tag{12}$$

Herein, J_e and J_ϑ denote the elastic and thermal part of the volumetric deformation. For the constitutive assumption of the thermal part J_ϑ see [51] with the temperature expansion coefficient α_T. Note, that α_T should not be confused with α representing the equivalent plastic strains in the elastoplasticity formulation, cf. Eq. (10). With view to finite plasticity, the spectral decomposition of the left Cauchy–Green tensor plays an important role, therefore, let us now consider

$$\boldsymbol{b}^e = \sum_{A=1}^{3} (\lambda_A^e)^2 \boldsymbol{n}_A \otimes \boldsymbol{n}_A, \tag{13}$$

cf. [80], with the eigenvalues λ_A^e and eigenvectors $\boldsymbol{n}_A$ of $\boldsymbol{b}^e$. With respect to the incorporation of initial volumetric strains we now consider the principle stresses in terms of the logarithmic principle strains $\epsilon_A^e = \ln \lambda_A^e$ with $A = 1, 2, 3$. For the volumetric isochoric split we obtain

$$\boldsymbol{\tau} = \kappa \operatorname{tr} \boldsymbol{\epsilon}^e \boldsymbol{1} + 2\mu \operatorname{dev} \boldsymbol{\epsilon}^e. \tag{14}$$

In order to incorporate initial (temperature) strains we need to modify the principle strains

$$\boxed{\epsilon_A^e \Leftarrow \epsilon_A^e - \alpha_T \vartheta}, \tag{15}$$

where $\alpha_T \vartheta$ represents the virtual temperature strains.

The remaining question is to identify the value of the virtual temperature strains such that a given volumetric strain is obtained. For the case of an initial (virtual) temperature strain in an unconstrained homogeneous specimen the volumetric stresses have to vanish ($\boldsymbol{\tau} = \boldsymbol{0}$). Exploiting Eq. (14) this means that the elastic strains have to vanish ($\boldsymbol{\epsilon}^e = \boldsymbol{0}$) and thus $J_e = 1$. Introducing the volume expansion ϵ_0 we obtain from Eq. (12)

$$1 + \epsilon_0 := J = J_\vartheta = e^{3\alpha_T \vartheta} \;\rightarrow\; \alpha_T \vartheta = \frac{1}{3} \ln(1 + \epsilon_0). \tag{16}$$

Note, that for the numerical implementation of the volume expansion in the used constitutive law, see Sect. 4.3.1, the two preceding equations play a central role. The modification of the principal strains due to the virtual temperature follows Eq. 15, wherein the virtual temperature strains $\alpha_T \vartheta$ are calculated by Eq. 16 with a prescribed volume expansion ϵ_0.

5.3.2 Locally distributed modification of ferritic yield law

As a result of the computation of initial volumetric strains in the martensite inclusions the distribution of equivalent plastic strains $\alpha_{IVS}(X)$ as a function of the position X in the microstructure is obtained. This is assumed to be associated with the eigenstrain state as a result of the production process when austenite transforms to martensite. We assume that these eigenstrains are correlated with the distribution of the hardness measure observed in the nanoindentation tests. Therefore, a shifted yield curve of the ferrite matrix phase is considered which is correlated with the distribution of the plastic eigenstrains $\alpha_{IVS}(X)$. This shift can be realized by increasing the material parameters y_0 and y_∞, i.e.,

$$y_0(X) \Leftarrow \gamma(X) \, y_0 \quad \text{and} \quad y_\infty(X) \Leftarrow \gamma(X) \, y_\infty, \tag{17}$$

with the definition for the modification factor

$$\gamma(X) := 1 + \overline{\gamma} \, \frac{\tilde{\alpha}_{IVS}(X)}{\langle \alpha_{IVS} \rangle}. \tag{18}$$

Herein, $\langle \alpha_{IVS} \rangle$ denotes the volumetric average of $\alpha_{IVS}(X)$ over the RVE and $\overline{\gamma}$ is a parameter for the DP steel that has to be determined by adjusting to experiments. In order to erase numerical singularities from the hardening modification, which are caused by singular values in the stress approximation insecurities at integration points, we introduce the expression

$$\tilde{\alpha}_{IVS}(X) := \begin{cases} \langle \alpha_{IVS} \rangle & \text{if} \quad \alpha_{IVS}(X) > \langle \alpha_{(IVS)} \rangle \\ \alpha_{IVS}(X) & \text{else.} \end{cases} \tag{19}$$

The modification of the hardening parameters y_0 and y_∞ is not only motivated by the existence of eigenstrain states, but also by the existence of areas of increased dislocation density and carbon content. In the hardness measurements shown in Fig. 14, the hardness close to the inclusions exceeds the hardness in the bulk by a maximal factor of approximately 1.6. Therefore, the modification parameter γ should be maximally 1.6, too, which leads to $\overline{\gamma} = 0.6$.

It should be mentioned that no grain size depending correction effecting the yielding of the ferritic phase according to Hall–Petch is explicitly considered in our approach. Finally, the internal modification parameter can therefore be interpreted as a combination of both effects, the hardness distribution as well as the Hall–Petch effect, that shifts the overall hardening curve of the DP steel.

5.3.3 Application of IVS to the SSMVEs

Now, we apply the previously described IVS approach to the volume-modified SSMVEs to assign a locally distributed yielding in the ferrite phase around the martensite inclusions. For that we apply volumetric strains as described in Sect. 5.3.1 to imply a volume expansion $\epsilon_0 = 4\,\%$, which is associated with a virtual thermal loading by $\alpha_T \vartheta \approx 0.01307$, cf. Eq. (16). Based on these results the initial yield strength and the asymptotic parameter are modified by the factor γ according to Eqs. (17) and (18). Note that motivated by the experimental results of the nano-indentation, cf. Fig. 14, the modification factor γ is bounded above by 1.6. Afterward we run the two uniaxial tensions tests in x- and z-direction, RD- and TD-direction, respectively, and compare the results with the experiments provided by ThyssenKrupp Steel Europe.

In Fig. 15 the distribution of the equivalent plastic strains and the von-Mises stresses after the application of the volumetric strains are shown. Due to the volumetric expansion of the martensite phase, the plasticized regions in the ferrite phase are mainly located around the inclusions and the plastic strains decrease with an increasing distance to the inclusions. Also between inclusions which are close together, a band with higher plastic strains can be observed. The distribution of the von-Mises stresses shows another effect, which will be taken into account considering the volume jump of the martensite phase. The increase in the volume results also to a locally nonzero stress state in the microstructure, which can be interpreted as residual stresses arising from the expansion of the martensite volume. These distributions of the equivalent plastic strains are used to
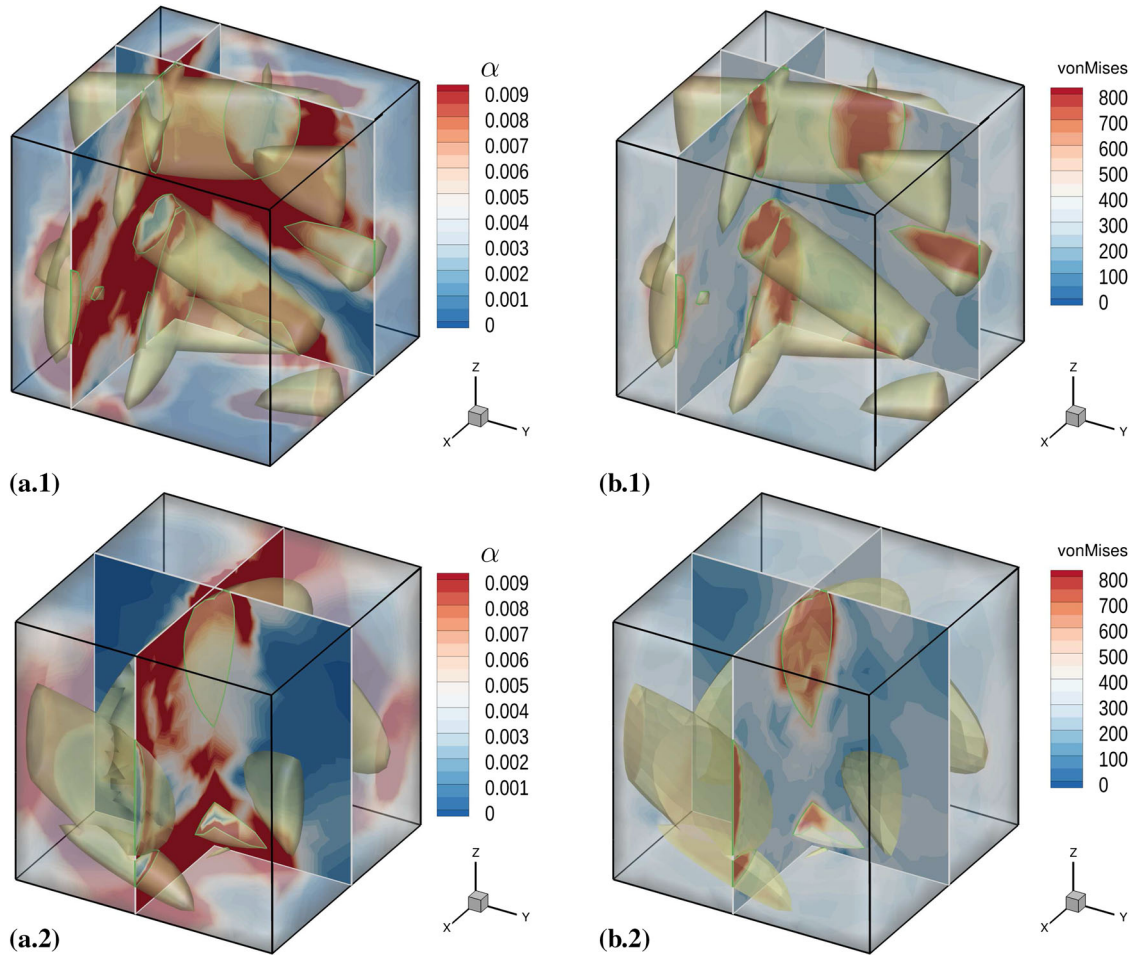
Fig. 15 Application of the IVS approach to (1) the SSMVE 1 and (2) the SSMVE 2: **a** distribution of the equivalent plastic strains α and **b** the von-Mises stresses at the full application of volumetric strains. The *bright yellow hulls* represent the volume of the martensite inclusions. The *green contours* characterize the edge of the interface between both the phases in the visualized cross sections. (Colour figure online)
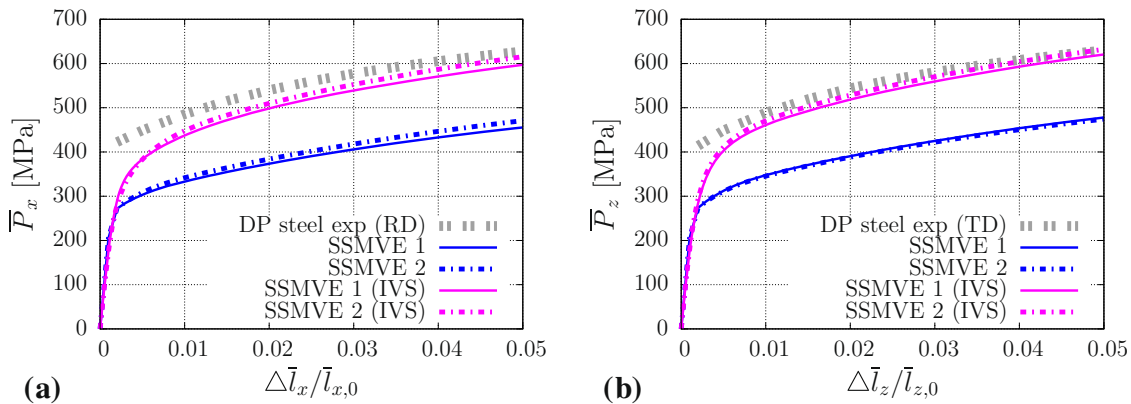
Fig. 16 Overall mechanical response, i.e., first Piola Kirchhofff stresses versus relative elongation, from uniaxial tension tests of the considered DP steel, volume-modified SSMVEs without and with IVS application, respectively. **a** RD-direction ($\overline{P}_x$ vs. $\triangle \overline{l}_x / \overline{l}_{x,0}$), **b** TD-direction ($\overline{P}_z$ vs. $\triangle \overline{l}_z / \overline{l}_{z,0}$). The experimental curves are provided by ThyssenKrupp Steel Europe

locally modify the ferrite yield curve. Then the computational uniaxial tension tests are performed in x- and z-directions associated with the RD- and TD-direction.

In Fig. 16 the result of the virtual experiments after the application of IVS are compared to the experimental results and the overall mechanical response of the SSMVEs without the application of IVS. The consideration of the IVS and the resulting local modification of the ferrite yield curve show good results with respect to the experimental data. Finally, the obtained SSMVE considering the martensite volume jump during the production process represent more suitable RVEs for two-scale simulations of DP steel applications.

Remark: An alternative to obtain SSVEs which may indeed be considered as representative is to directly combine statistical information from the *Largescan* and the *Slicescan* when defining the objective function $\mathcal{E}$. Then least-square functionals based on a *Largescan* e.g., standard basic scalar-valued descriptors, and least-square functionals based on a *Slicescan*, e.g., considering spectral density and/or lineal-path function, are reasonably weighted to directly obtain a SSVE, which incorporates statistical information obtained from different measurement techniques.

6 Conclusions

In this paper the construction of representative microstructures was analyzed for the application in two-scale simulations of DP steels. The basis was the measurement of the microstructural information by 3D EBSD/FIB and 2D EBSD large area scans. It turned out that the martensite phase fraction of the three-dimensional reconstructions were significantly lower ($\approx 9\%$), as the ensemble average of multiple small 2D area scans ($\approx 14.4\%$). Also the computational two-scale simulations using the discretization of the three-dimensional structures shared large deviations to the results of mechanical experiments with the real material. In order to achieve an improved computational efficiency in two-scale simulations compared to "standard" RVEs, which are mostly a partial volume of the real material, we concentrated on statistically similar volume elements (SSVEs). First SSVEs were constructed for the raw three-dimensional reconstruction. Then the martensite phase fraction in these SSVEs was adjusted to the reference value to obtain volume-modified SSMVEs. Thereby an additional advantage of the SSVEs became clear: due to the parametrization of their morphology by three ellipsoids only their radii had to be sufficiently increased to adjust for the increase volume fraction. This is rather simple compared to the large effort which would be necessary for the real geometrically complex structure. Numerical tests showed a slight improvement and still a large gap to the experimental results. Consequently, some physical effects at the microscale were not already captured by the numerical model. Nanoindentation tests revealed that the assumption of constant material properties in the ferritic matrix is not valid. It turned out that the hardness increases exponentially when approaching the martensitic inclusion. Possible reasons were assumed to be accumulations of dislocations and locally different carbon content due to the production process, where a volume expansion of the inclusions is induced by phase transformation. To capture these distributed properties, a volumetric expansion in the inclusions was taken into account. The arising equivalent plastic strain distribution in the ferrite phase provided the basis for a locally distributed modification of the ferritic yield curve. The numerical simulations considering the distributed yield behavior in the ferrite phase due to this approach showed good accordance with the experimental results.

References

1. Al-Abbasi, F.M., Nemes, J.A.: Micromechanical modeling of dual phase steels. Int. J. Mech. Sci. **45**(9), 1449–1465 (2003a)
2. Al-Abbasi, F.M., Nemes, J.A.: Micromechanical modeling of the effect of particle size difference in dual phase steels. Int. J. Solids Struct. **40**(13–14), 3379–3391 (2003b)
3. Al-Abbasi, F.M., Nemes, James A.: Characterizing dp-steels using micromechanical modeling of cells. Comput. Mater. Sci. **39**(2), 402–415 (2007)
4. Ambrozinski, M., Bzowski, K., Rauch, L., Pietrzyk, M.: Application of statistically similar representative volume element in numerical simulations of crash box stamping. Arch. Comput. Methods Eng. **12**, 126–132 (2012)

5. Avramovic-Cingara, G., Ososkov, Y., Jain, M.K., Wilkinson, D.S.: Effect of martensite distribution on damage behaviour in DP600 dual phase steels. Mater. Sci. Eng. A **516**(1–2), 7–16 (2009)
6. Balzani, D., Schröder, J., Brands, D.: FE^2-simulation of microheterogeneous steels based on statistically similar RVE's. In: Proceedings of the IUTAM Symposium on Variational Concepts with Applications to the Mechanics of Materials, Bochum, Germany (2008)
7. Balzani, D., Brands, D., Schröder, J., Carstensen, C.: Sensitivity analysis of statistical measures for the reconstruction of microstructures based on the minimization of generalized least-square functionals. Technische Mechanik **30**, 297–315 (2010)
8. Balzani, D., Brands, D., Schröder, J.: Construction of statistically similar representative volume elements. In: Schröder, J., Hackl, K. (eds) Plasticity and Beyond, vol. 550 of CISM Courses and Lectures, pp. 355–412. Springer
9. Balzani, D., Scheunemann, L., Brands, D., Schröder, J.: Construction of two- and three-dimensional statistically similar RVEs for coupled micro-macro simulations. Comput. Mech. **54**(5), 1269–1284 (2014b)
10. Beran, M.: Statistical Continuum Theories. Wiley, New York (1968)
11. Bhandari, Y., Sarkar, S., Groeber, M., Uchic, M.D., Dimiduk, D.M., Ghosh, S.: 3d polycrystalline microstructure reconstruction from FIB generated serial sections for FE analysis. Comput. Mater. Sci. **41**(2), 222–235 (2007)
12. Black, M.P., Higginson, R.L.: An investigation into the use of electron back scattered diffraction to measure recrystallised fraction. Scripta Mater. **41**(2), 125–129 (1999)
13. Brahme, A., Alvi, M.H., Saylor, D., Fridy, J., Rollett, A.D.: 3d reconstruction of microstructure in a commercial purity aluminum. Scripta Mater. **55**(1), 75–80 (2006)
14. Brands, D., Balzani, D., Schröder, J., Raabe, D.: Simulation of DP-steels based on statistically similar representative volume elements and 3D EBSD data. In: Computational Plasticity XI—Fundamentals and Applications, pp. 1552–1563, Barcelona, Spain, (2011)
15. Calcagnotto, M., Ponge, D., Demir, E., Raabe, D.: Orientation gradients and geometrically necessary dislocations in ultrafine grained dual-phase steels studied by 2d and 3d EBSD. Mater. Sci. Eng. A **527**(10–11), 2738–2746 (2010)
16. Calcagnotto, M., Adachi, Y., Ponge, D., Raabe, D.: Deformation and fracture mechanisms in fine- and ultrafine-grained ferrite/martensite dual-phase steels and the effect of aging. Acta Mech. **59**, 658–670 (2011)
17. Choi, S.-H., Kim, D.W., Seong, B.S., Rollett, A.D.: 3-d simulation of spatial stress distribution in an AZ31 Mg alloy sheet under in-plane compression. Int. J. Plast **27**(10), 1702–1720 (2011)
18. Choi, S.-H., Kim, E.-Y., Woo, W., Han, S.H., Kwak, J.H.: The effect of crystallographic orientation on the micromechanical deformation and failure behaviors of DP980 steel during uniaxial tension. Int. J. Plast **45**, 85–102 (2013)
19. Das, D., Chattopadhyay, P.P.: Influence of martensite morphology on the work-hardening behavior of high strength ferrite-martensite dual-phase steel. J. Mater. Sci. **44**(11), 2957–2965 (2009)
20. Davies, R.G.: Influence of martensite composition and content on the properties of dual phase steels. Metall. Mater. Trans. A **9**, 671–679 (1978)
21. Davut, K., Zaefferer, S.: Statistical reliability of phase fraction determination based on electron backscatter diffraction (EBSD) investigations on the example of an Al-TRIP steel. Metall. Mater. Trans. A **41**(9), 2187–2196 (2010)
22. Davut, K., Zaefferer, S.: Improving the reliability of EBSD-based texture analysis by a new large area mapping technique. Mater. Sci. Forum **702–703**, 566–569 (2012)
23. Demir, E., Raabe, D., Zaafarani, N., Zaefferer, S.: Investigation of the indentation size effect through the measurement of the geometrically necessary dislocations beneath small indents of different depths using EBSD tomography. Acta Mater. **57**(2), 559–569 (2009)
24. Diard, O., Leclercq, S., Rousselier, G., Cailletaud, G.: Evaluation of finite element based analysis of 3d multicrystalline aggregates plasticity: Application to crystal plasticity model identification and the study of stress and strain fields near grain boundaries. Int. J. Plast **21**(4), 691–722 (2005)
25. Drugan, W.J., Willis, J.R.: A micromechanics-based nonlocal constitutive equation and estimates of representative volume element size for elastic composites. J. Mech. Phys. Solids **44**, 497–524 (1996)
26. Eisenlohr, P., Diehl, M., Lebensohn, R.A., Roters, F.: a spectral method solution to crystal elasto-viscoplasticity at finite strains. Microstructure-based models of plastic deformation. Int. J. Plast **46**, 37–53 (2013)
27. Exner, H.E., Hougardy, H.P.: Einführung in die quantitative Gefügeanalyse. Deutsche Gesellschaft für Metallkunde (1986)
28. Feyel, F.: Multiscale FE^2 elastoviscoplastic analysis of composite structures. Comput. Mater. Sci. **16**, 344–354 (1999)
29. Gerber, P.H., Tarasiuk, J., Chiron, R., Bacroix, B.: Estimation of the recyrstallized volume fraction from local misorientation calculations. Arch. Metall. Mater. **50**(5), 747–755 (2005)
30. Ghosh, S., Bhandari, Y., Groeber, M.: CAD-based reconstruction of 3d polycrystalline alloy microstructures from FIB generated serial sections. Comput. Aided Des. **40**(3), 293–310 (2008)
31. Groeber, M.A., Haley, B.K., Uchic, M.D., Dimiduk, D.M., Ghosh, S.: 3d reconstruction and characterization of polycrystalline microstructures using a fib-sem system. Mater. Charact. **57**(4–5), 259–273 (2006)
32. Hashin, Z.: Analysis of composite materials—a survey. J. Appl. Mech. **50**, 481–505 (1983)
33. He, B.B., Huang, M.X.: Revealing the intrinsic nanohardness of lath martensite in low carbon steel. Metall. Mater. Trans. A **46**(2), 688–694 (2015)
34. Hill, R.: Elastic properties of reinforced solids: some theoretical principles. J. Mech. Phys. Solids **11**, 357–372 (1963)
35. Jeong, B.-Y., Gauvin, R., Yue, S.: EBSD study of martensite in a dual phase steel. Microsc. Microanal. **8**, 700–701 (2002)
36. Jeong, B.Y., Ryou, M., Lee, C., Kim, M.H.: A study on the surface characteristics of dual phase steel by electron backscatter diffraction EBSD technique. Trans. Electr. Electr. Mater. **15**(1), 20–23 (2014)
37. Kadkhodapour, J., Butz, A., Ziaei-Rad, S., Schmauder, S.: A micro mechanical study on failure initiation of dual phase steels under tension using single crystal plasticity model. Int. J. Plast **27**(7), 1103–1125 (2011a)
38. Kadkhodapour, J., Schmauder, S., Raabe, D., Ziaei-Rad, S., Weber, U., Calcagnotto, M.: Experimental and numerical study on geometrically necessary dislocations and non-homogeneous mechanical properties of the ferrite phase in dual phase steels. Acta Mater. **59**(11), 4387–4394 (2011b)

39. Kang, J., Ososkov, Y., Embury, J.D., Wilkinson, D.S.: Digital image correlation studies for microscopic strain distribution and damage in dual phase steels. Scripta Mater. **56**(11), 999–1002 (2007)
40. Khan, A.S., Baig, M., Choi, S.-H., Yang, H.-S., Sun, X.: Quasi-static and dynamic responses of advanced high strength steels: experiments and modeling. Int. J. Plast **30–31**, 1–17 (2012)
41. Kim, N.J., Thomas, G.: Effects of morphology on the mechanical behavior of a dual phase Fe/2Si/0.1C steel. Metall. Trans. A **12A**, 483–489 (1981)
42. Kim, S., Lee, S.: Effects of martensite morphology and volume fraction on quasi-static and dynamic deformation behavior of dual-phase steels. Metall. Mater. Trans. A **31**(7), 1753–1760 (2000)
43. Klinkel, S.: Theorie und Numerik eines Volumen-Schalen-Elementes bei finiten elastischen und plastischen Verzerrungen. In: Dissertation thesis, Institut für Baustatik, Universität Karlsruhe (2000)
44. Konrad, J., Zaefferer, S., Raabe, D.: Investigation of orientation gradients around a hard laves particle in a warm rolled fe3al-based alloy by a 3d ebsd-fib technique. Acta Mech. **54**, 1369–1380 (2006)
45. Koo, J.K., Thomas, G.: Thermal cycling treatments and microstructures for improved properties of Fe-0.12% C-0.5% Mn steels. Mater. Sci. Eng. **24**, 187–198 (1976)
46. Kröner, E.: Allgemeine Kontinuumstheorie der Versetzung und Eigenspannung. Arch. Ration. Mech. Anal. **4**, 273–334 (1960)
47. Kröner, E.: Statistical continuum mechanics. In: CISM Courses and Lectures, vol 92. Springer, Wien, (1971)
48. Lee, E.H.: Elasto-plastic deformation at finite strains. J. Appl. Mech. **36**, 1–6 (1969)
49. Lee, S.-B., Lebensohn, R.A., Rollett, A.D.: Modeling the viscoplastic micromechanical response of two-phase materials using fast fourier transforms. Int. J. Plast **27**(5), 707–727 (2011)
50. Lewis, A.C., Geltmacher, A.B.: Image-based modeling of the response of experimental 3d microstructures to mechanical loading. Scripta Mater. **55**(1), 81–85 (2006)
51. Lu, S.C.H., Pister, K.S.: Decomposition of deformation and representation of the free energy function for isotropic thermoelastic solids. Int. J. Solids Struct. **11**(7–8), 927–934 (1975)
52. Mediratta, S.R., Ramaswamy, V., Rao, P.R.: Influence of ferrite-martensite microstructural morphology on the low cycle fatigue of a dual-phase steel. Int. J. Fatigue **7**(2), 107–115 (1985)
53. Miehe, C.: Kanonische Modelle multiplikativer Elasto-Plastizität. Thermodynamische Formulierung und Numerische Implementation. In: Habilitation Thesis, Universität Hannover, Institut für Baumechanik und Numerische Mechanik, Report No. F93/1 (1993)
54. Miehe, C., Stein, E.: A canonical model of multiplicative elasto-plasticity formulation and aspects of the numerical implementation. Eur. J. Mech. A Solids **11**, 25–43 (1992)
55. Miehe, C., Schotte, J., Schröder, J.: Computational micro-macro-transitions and overall moduli in the analysis of polycrystals at large strains. Comput. Mater. Sci. **16**, 372–382 (1999a)
56. Miehe, C., Schröder, J., Schotte, J.: Computational homogenization analysis in finite plasticity. Simulation of texture development in polycrystalline materials. Comput. Methods Appl. Mech. Eng. **171**, 387–418 (1999b)
57. Moyer, J.M., Ansell, G.S.: The volume expansion accompanying the martensite transformation in iron–carbon alloys. Metall. Trans. A **6**(9), 1785–1791 (1975)
58. O'Haver, T.: Peak Fitter. MATLAB Central File Exchange, 2013. URL http://www.mathworks.com/matlabcentral/fileexchange/23611-peak-fitter. Version 3.6: February, 2013; retrieved at April 22 (2013)
59. Ohser, J., Mücklich, F.: Statistical Analysis of Microstructures in Materials Science. Wiley, New York (2000)
60. Ostoja-Starzewski, M.: The use, misuse, and abuse of stochastic random media. In: Proceedings of European Conference on Computational Mechanics (2001)
61. Park, S.H.: Microstructural evolution of hot rolled trip steels during cooling control. In: 40th Mechanical Working and Steel Processing Conference. ISS/ AIME, pp. 283–291, Pittsburgh (1998)
62. Paul, S.K.: Micromechanics based modeling of dual phase steels: prediction of ductility and failure modes. Comput. Mater. Sci. **56**, 34–42 (2012)
63. Paul, S.K.: Effect of martensite volume fraction on stress triaxiality and deformation behavior of dual phase steel. Mater. Design **50**, 782–789 (2013a)
64. Paul, S.K.: Real microstructure based micromechanical model to simulate microstructural level deformation behavior and failure initiation in DP 590 steel. Mater. Design **44**, 397–406 (2013b)
65. Peranio, N., Li, Y.J., Roters, F., Raabe, D.: Microstructure and texture evolution in dual-phase steels: competition between recovery, recrystallization, and phase transformation. Mater. Sci. Eng. A **527**(16–17), 4161–4168 (2010)
66. Peric, D., Owen, D.R.J., Honnor, M.E.: A model for finite strain elasto-plasticity based on logarithmic strains: computational issues. Comput. Methods Appl. Mech. Eng. **94**, 35–61 (1992)
67. Rice, P.M., Stoller, R.E.: Correlation of nanoindentation and conventional mechanical property measurements. In: Symposium Q- Fundamentals of Nanoindentation & Nanotribology II, vol 649 of MRS Proceedings, 1 (2000)
68. Rollett, A.D., Campman, R., Saylor, D.: Three dimensional microstructures: statistical analysis of second phase particles in AA7075-T651. Mater. Sci. Forum **519–521**, 1–10 (2006)
69. Rollett, A.D., Lee, S.-B., Campman, R., Rohrer, G.S.: Three-dimensional characterization of microstructure by electron back-scatter diffraction. Annu. Rev. Mater. Res. **37**(1), 627–658 (2007)
70. Orsetti Rossi, P.L., Sellars, C.M.: Quantitative metallography of recrystallization. Acta Mech. **45**(1), 137–148 (1997)
71. Sakaki, T., Sugimoto, K., Fukuzato, T.: Role of internal stress for continuous yielding of dual-phase steels. Acta Metall. **31**(10), 1737–1746 (1983)
72. Saylor, D.M., Fridy, J., El-Dasher, B.S., Jung, K.-Y., Rollett, A.D.: Statistically representative three-dimensional microstructures based on orthogonal observation sections. Metall. Mater. Trans. A **35**(7), 1969–1979 (2004)
73. Scheunemann, L., Balzani, D., Brands, D., Schröder, J.: Design of 3d statistically similar representative volume elements based on minkowski functionals. Mech. Mater. (2015). doi:10.1016/j.mechmat.2015.03.005

74. Schröder, J.: Homogenisierungsmethoden der nichtlinearen Kontinuumsmechanik unter Beachtung von Stabilitätsproblemen. In: Habilitation Thesis, Bericht aus der Forschungsreihe des Institut für Mechanik (Bauwesen), Lehrstuhl I, Universität Stuttgart (2000)

75. Schröder, J.: Plasticity and beyond—microstructures, crystal-plasticity and phase transitions. In: Schröder, J., Hackl, K. (eds.) CISM Lecture Notes 550, chapter A Numerical Two-scale Homogenization Scheme: The FE^2-method. Springer (2014)

76. Schröder, J., Balzani, D.: Meso-macro modeling of multiphase steels based on the FE^2-method. In: Internal Report 52, Institut für Mechanik, Fakultät für Ingenieurwissenschaften, Universität Duisburg-Essen, Germany (2010)

77. Schröder, J., Balzani, D., Richter, H., Schmitz, P. H., Kessler, L.: Simulation of microheterogeneous steels based on a discrete multiscale approach. In: Numisheet 2008: Proceedings of the 7th International Conference and Workshop on Numerical Simulation of 3d Sheet Metal Forming Processes (2008)

78. Schröder, J., Balzani, D., Brands, D.: Approximation of random microstructures by periodic statistically similar representative volume elements based on lineal-path functions. Arch. Appl. Mech. **81**(7), 975–997 (2011)

79. Simo, J.C.: A framework for finite strain elastoplasticity based on maximum plastic dissipation and the multiplicative decomposition: Part I. Continuum formulation. Comput. Methods Appl. Mech. Eng. **66**, 199–219 (1988)

80. Simo, J.C.: Algorithms for static and dynamic multiplicative plasticity that preserve the classical return mapping schemes of the infinitesimal theory. Comput. Methods Appl. Mech. Eng. **99**, 61–112 (1992)

81. Simo, J.C., Miehe, C.: Associative coupled thermoplasticity at finite strains: formulation, numerical analysis and implementation. Comput. Methods Appl. Mech. Eng. **96**, 133–171 (1992)

82. Smit, R.J.M., Brekelmans, W.A.M., Meijer, H.E.H.: Prediction of the mechanical behavior of nonlinear heterogeneous systems by multi-level finite element modeling. Comput. Methods Appl. Mech. Eng. **155**, 181–192 (1998)

83. St-Pierre, L., Héripré, E., Dexet, M., Crépin, J., Bertolino, G., Bilger, N.: 3d simulations of microstructure and comparison with experimental microstructure coming from o.i.m analysis. Int. J. Plast **24**(9), 1516–1532 (2008)

84. Stroeven, M., Askes, H., Sluys, L.J.: A numerical approach to determine representative volumes for granular materials. In: Fifth World Congress on Computational Mechanics (WCCM V). Vienna University of Technology (2002)

85. Sung, J.H., Kim, J.H., Wagoner, R.H.: A plastic constitutive equation incorporating strain, strain-rate, and temperature. Int. J. Plast **26**(12), 1746–1771 (2010)

86. Tarasiuk, J., Gerber, P.H., Bacroix, B.: Estimation of recrystallized volume fraction from EBSD data. Acta Mater. **50**(6), 1467–1477 (2002)

87. Tasan, C.C., Diehl, M., Yan, D., Zambaldi, C., Shanthraj, P., Roters, F., Raabe, D.: Integrated experimental-simulation analysis of stress and strain partitioning in multiphase alloys. Acta Mater. **81**, 386–400 (2014a)

88. Tasan, C.C., Hoefnagels, J.P.M., Diehl, M., Yan, D., Roters, F., Raabe, D.: Strain localization and damage in dual phase steels investigated by coupled in-situ deformation experiments and crystal plasticity simulations. Int. J. Plast **63**, 198–210 (2014b)

89. Temizer, I., Wriggers, P.: On the computation of the macroscopic tangent for multiscale volumetric homogenization problems. Comput. Methods Appl. Mech. Eng. **198**, 495–510 (2008)

90. Tomita, Y.: Effect of morphology of second-phase martensite on tensile properties of Fe-0.1C dual phase steels. J. Mater. Sci. **25**(12), 5179–5184 (1990)

91. Torquato, S.: Random Heterogeneous Materials. Microstructure and Macroscopic Properties. Springer, Berlin (2002)

92. Uchic, M.D.: Serial sectioning methods for generating 3d characterization data of grainand precipitate-scale microstructures. In: Ghosh, S., Dimiduk, D. (eds.) Computational Methods for Microstructure-Property Relationships, pp. 31–52. Springer, Berlin (2011)

93. Uthaisangsuk, V., Prahl, U., Bleck, W.: Modelling of damage and failure in multiphase high strength DP and TRIP steels. Eng. Fract. Mech. **78**(3), 469–486 (2011)

94. Voce, E.: A practical strain hardening function. Metallurgica **51**, 219–226 (1955)

95. Weber, G., Anand, L.: Finite deformation constitutive equations and a time integration procedure for isotropic, hyperelastic-viscoelastic solids. Comput. Methods Appl. Mech. Eng. **79**, 173–202 (1990)

96. Wilkinson, A.J., Dingly, D.J.: Quantitative deformation studies using electron back scatter patterns. Acta Metall. Mater. **39**, 3047–3055 (1991)

97. Wilson, A.W., Spanos, G.: Application of orientation imaging microscopy to study phase transformations in steels. Mater. Charact. **46**, 407–418 (2001)

98. Wilson, A.W., Madison, J.D., Spanos, G.: Determining phase volume fraction in steels by electron backscattered diffraction. Scripta Mater. **45**, 1335–1340 (2001)

99. Wright, S.I., Nowell, M.M.: EBSD image quality mapping. Microsc. Microanal. **12**, 72–84 (2006)

100. Wu, J., Wray, P.J., Garcia, C.I., Hua, M., Deardo, A.J.: Image quality analysis: a new method of characterizing microstructures. ISIJ Int. **45**, 254–262 (2005)

101. Zaafarani, N., Raabe, D., Singh, R.N., Roters, F., Zaefferer, S.: Three-dimensional investigation of the texture and microstructure below a nanoindent in a cu single crystal using 3d EBSD and crystal plasticity finite element simulations. Acta Mater. **54**(7), 1863–1876 (2006)

102. Zaefferer, S., Wright, S.I., Raabe, D.: Three-dimensional orientation microscopy in a focused ion beam-scanning electron microscope: a new dimension of microstructure characterization. Metall. Mater. Trans. A **39**(2), 374–389 (2008)

103. Zeman, J.: Analysis of composite materials with random microstructure. In: PhD Thesis, University of Prague (2003)